Copy 6
RM A51H20a

NACA RM A51H20a

NACA

RESEARCH MEMORANDUM

COMPARISON OF DRAG, PRESSURE RECOVERY, AND SURFACE PRESSURE OF A SCOOP-TYPE INLET AND AN NACA SUBMERGED INLET AT TRANSONIC SPEEDS

By Joseph L. Frank and Robert A. Taylor

Ames Aeronautical Laboratory
Moffett Field, Calif.

NATIONAL ADVISORY COMMITTEE
FOR AERONAUTICS

WASHINGTON

December 17, 1951

NATIONAL ADVISORY COMMITTEE FOR AERONAUTICS

RESEARCH MEMORANDUM

COMPARISON OF DRAG, PRESSURE RECOVERY, AND SURFACE PRESSURE OF A SCOOP-TYPE INLET AND AN NACA SUBMERGED INLET AT TRANSONIC SPEEDS

By Joseph L. Frank and Robert A. Taylor

SUMMARY

A solid half body was modified to mount first a scoop inlet and then an NACA submerged inlet while maintaining the same entrance geometry, afterbody, and diffuser for both inlets. The model was mounted on the transonic bump of the Ames 16-foot high-speed wind tunnel and was tested through an angle-of-attack range of 0° to 9° and a Mach number range of 0.79 to 1.12. The range of mass-flow ratio was from 0 to a maximum of 0.92. Comparative pressure-recovery, pressure-distribution, and drag data were obtained for the two inlet types.

At the low mass-flow ratios, the submerged inlet always gave higher ram recovery than did the scoop inlet. This is attributed to the thicker growth of boundary layer along the approach of the scoop inlet. At the maximum mass-flow ratio, ram recovery of the scoop and the submerged inlets was about the same at 0° angle of attack. The effect of Mach number was small on both inlet types but Mach number effects augmented the adverse effects of angle of attack on the submerged inlet.

Total drag was about the same for both inlets except at 6° angle of attack where the total drag of the scoop inlet was higher. The increment of external drag was higher for the scoop inlet up to Mach numbers of 1.08 at 0° and at all Mach numbers at 6°.

INTRODUCTION

The scoop-type inlet and the NACA submerged inlet are two current inlet designs which supply air to a jet engine and require a relatively short internal ducting. An NACA submerged inlet has been previously tested at transonic speeds (references 1 and 2), but no previous

transonic tests of a scoop inlet are known. The purpose of this investigation was to compare the transonic characteristics of a scoop-type inlet with those of a submerged inlet. To provide a basis of comparison, the inlets were each mounted in the same half body, the model being identical from the leading edge of the entrance lip rearward with either inlet mounted in the body. The model was tested on the transonic bump of the Ames 16-foot high-speed wind tunnel. The average Mach number over the bump test section ranged from 0.79 to 1.12.

SYMBOLS

A	inlet area, square feet
d	maximum depth of inlet entrance, 0.95 inch
H	total pressure, pounds per square foot
h	boundary-layer parameter designating the height for which a complete loss of dynamic pressure would be equivalent to the integrated loss of total pressure in the actual boundary layer $\left[\frac{1}{H_o - p_o}\int_o^{\delta}(H_o - H)dy\right]$, inches
M	Mach number
m	mass flow (ρVA), slugs per second
P	pressure coefficient $\left(\frac{p - p_o}{q_o}\right)$
P_{cr}	critical pressure coefficient (the pressure coefficient corresponding to sonic velocity)
p	static pressure, pounds per square foot
q	dynamic pressure ($\frac{1}{2}\rho V^2$), pounds per square foot
S	maximum frontal area of half model, 0.0681 square feet
V	velocity outside the boundary layer, feet per second

[redacted]

v local velocity in the boundary layer, feet per second

y ordinate perpendicular to ramp surface at station of boundary-layer measurement, inches

C_D drag coefficient $\left(\frac{\text{drag}}{q_o 2S}\right)$

C_{D_i} internal drag coefficient $\left[C_{D_i} = \frac{\int_{\text{wake}} \rho_2 V_2 (V_o - V_3) dA_2}{q_o \, 2S}\right]$

ΔC_{D_E} increment of external drag coefficient due to the air induction system $\left(\Delta C_{D_E} = C_{D_T} - C_{D_S} - C_{D_i}\right)$

C_{D_S} total drag coefficient of model with solid nose and tail cone

C_{D_T} total drag coefficient of model with an inlet in place

$\frac{H_1 - p_o}{H_o - p_o}$ ram-recovery ratio at the entrance

$\frac{m_1}{m_o}$ ratio of the mass flow through the inlet to the mass flow in the free stream through an area equal to the inlet area $\left(\frac{\rho_1 A_1 V_1}{\rho_o A_1 V_o}\right)$

α angle of attack of the model, degrees

δ boundary-layer thickness where the local velocity is 0.99 of the velocity outside the boundary layer, inches

ρ mass density, slugs per cubic foot

[redacted]

Subscripts

o	free stream
1	inlet rake
2	diffuser exit
3	station downstream of the exit where $p_3 = p_o$

TESTS

The range of free-stream Mach numbers of this test was from 0.79 to 1.12, corresponding under the test conditions to a Reynolds number range from 3.7 to 4.4 million per foot of length. Due to the streamwise gradient of Mach number along the bump, the free-stream Mach number was taken as the average Mach number between a station 3 inches in front of the model and a station 2 inches behind the model. These local Mach numbers were measured along the bump surface away from the influence of of the model. Also, because of the streamwise gradient, the free-stream factors used in the calculation of pressure coefficients. (q_o and p_o) were local free-stream values.

The test angles of attack were 0°, 3°, 6°, and 9°. To provide a range of mass-flow ratio, constrictions were inserted at the model exit, providing exit-area ratios of 1 (full open), 3/4, 1/4, and 0 (plugged). Pressure recovery and mass flow at the inlet rake were measured at 0° and 6° angle of attack for the full range of exit-area ratios. At 3° and 9° they were measured only with the exit full open. Pressure distribution was recorded with the exit full open for 0°, 6°, and 9° angle of attack; drag measurements were made with the outlet full open and plugged at 0°, 3°, 6°, and 9°. With the exit full open, boundary-layer measurements were made at 0° angle of attack and tuft photographs were made at 0° and 9°.

MODEL AND APPARATUS

A complete description and photographs of the transonic bump were given in reference 1 along with distributions of local Mach number over the surface of the bump.

Three basic models were tested in this investigation: they were the solid body, the body with the scoop inlet, and the body with the NACA

submerged inlet. Photographs of the models mounted on the transonic bump are presented in figure 1. The scoop model and the submerged model were fabricated by modification of the solid-nose body forward of the station corresponding to the leading edge of the entrance lip. Thus, all three models were identical from the entrance lip to the diffuser exit. The same tail cone was used to complete the solid body and to plug the exit of the body with inlet installed. Details and dimensions of the three noses and of the single fuselage afterbody are given in figures 2 and 3.

Internal diffusion of the air from either the scoop or the submerged inlet began 0.40 inch behind the lip leading edge (where the lip curvature ended) and continued to within 1 inch of the exit. The entrance area was 2 square inches and the maximum exit area was 3.14 square inches. To avoid the boundary layer of the bump, all models were tested 3/4 inch from the bump surface. Beneath the model was an underbody (fig. 2) that was fastened to the bump surface and cleared the bottom of the model by about 1/8 inch. The model was supported from the bump by a strut that projected through the underbody.

An inlet rake was in the duct 2.75 inches behind the leading edge of the entrance lip. It was composed of 19 total-pressure tubes and 14 static-pressure tubes, the total-pressure tubes being disposed so as to be located in the center of approximately equal areas. Data from the inlet rake were used to compute ram-recovery and mass-flow ratios. An exit rake was mounted on the bump surface 1/2 inch behind the model exit. It was composed of 37 total-pressure tubes and 4 static-pressure tubes spaced along two mutually perpendicular diameters and provided data for the calculation of internal drag. The location of the tubes in the exit rake is shown in figure 4. Total drag of the models was measured by a strain-gage balance located within the bump.

The boundary layer was measured by a rake centered 1/2 inch in front of the entrance. For test conditions with a thickened boundary layer, a 1/2-inch-wide strip of mucilage impregnated with fine carborundum was located 5 inches behind the nose of the model. Flush pressure orifices were located along the body and the inside of the entrance lip, as indicated in figure 5.

REDUCTION OF DATA

The ram-recovery ratio at the entrance was calculated from the measured pressures by the method derived in reference 3. The logarithm of the total pressure at each of the 19 tubes in the entrance rake was weighted by the mass flow through the area assigned to that tube.

[redacted]

The mass-flow ratio was computed from the summation of the mass flows through the 19 equal areas.

The relative merit of various methods of weighting the pressures over the area of a duct to determine an average or effective value of the total pressure is a subject of controversy. Area-averaging, mass-flow averaging, and other methods have been proposed and used by different authors. A comparison of these methods indicates that all of them give results within 1 or 2 percent of each other for relatively uniform total-pressure distributions. For extreme distributions, with large peaks and hollows, these various methods may lead to widely different results and it has not yet been established that any of these are accurate for engineering purposes. In view of the fact that in the cases of most practical interest the various methods yield similar results, the labor involved in computing results by several methods did not seem warranted.

The coefficient of internal drag was calculated by the method outlined in reference 4 and is essentially a measurement of change in momentum of the air from the free stream to the station of measurement. Figure 4 presents a typical plot of point-drag coefficient across the exit of the model, including both internal and external drag influences. The portion of the drag data that was assumed to be due to internal flow and which was used in calculation of internal drag coefficient is indicated. Such an assumption is considered to be reasonable for the comparative values of drag coefficient that are presented for the two inlets. The increment of external drag coefficient was calculated by subtracting the coefficient of solid-body drag and of internal drag from the coefficient of total drag of the body with inlet. It reflects the change in the external drag due to the air-induction system. All drag coefficients were based on twice the maximum frontal area of the half body.

RESULTS

The figures presenting results in this report fall into five general classifications. These classifications and the figures within each classification are listed as follows:

[redacted]

Classification	Figures
Variation of ram-recovery ratio:	
Variation of ram-recovery ratio and mass-flow ratio with Mach number	6, 7
Cross plots of ram-recovery ratio versus mass-flow ratio	8, 9
Contours of ram-recovery ratio and mass-flow ratio	10 to 14
Boundary-layer parameters	15, 16
Tuft pictures	17, 18
Distribution of pressure coefficient	19 to 27
Variation of drag coefficient	28 to 32

DISCUSSION

Ram-Recovery Ratio

Effect of mass-flow ratio.- For comparison at equal mass-flow ratios, the data of figures 6 and 7 (where both mass-flow ratio and Mach number vary) are cross-plotted in figures 8 and 9. Curves of ram-recovery ratio versus mass-flow ratio for the scoop and submerged inlets (figs. 8 and 9) all showed low ram recovery at low mass-flow ratios. The scoop ram recovery was always lower than the recovery with the submerged inlet at low mass-flow ratios due, it is believed, to the thicker growth of boundary layer along the approach of the scoop inlet as compared to that along the ramp of the submerged inlet. The much lower rate of boundary-layer growth along the ramp of a submerged inlet with diverging ramp walls (similar to the one of this investigation) compared to that of a submerged inlet with parallel ramp walls was shown in reference 5. The submerged inlet with parallel walls can be considered to approach a scoop design.

At the maximum mass-flow ratios, the ram recoveries of the scoop and submerged inlets were about the same at 0° angle of attack (figs. 8 and 9). The fact that the scoop had equal ram recovery even though a thicker boundary layer was measured (fig. 15) was due to low-energy air entering the submerged inlet at the corners near the lip,

[redacted]

the entrance of such air not registering on the boundary-layer rake at the entrance center line. The presence of the low-energy air is indicated in the contours of figure 12 by the areas of low ram recovery at the corners near the lip. The low-energy air is believed to be due to vortex formation off the diverging walls of the ramp and to fuselage boundary layer that these vortices carried into the corners of the entrance. Photographs of such vortex formation on a submerged inlet were presented in reference 5.

Effect of angle of attack and Mach number.- Although at low angles of attack and subsonic Mach numbers the submerged inlet had equal or higher ram recovery, increasing angle of attack had a more adverse effect on ram recovery of the submerged inlet than on that of the scoop inlet (figs. 8 and 9), such adverse effect on the submerged inlet beginning at lower angle of attack as Mach number increased. The more adverse effect of increasing angle of attack on the submerged inlet is attributed to the increasing strength of the vortex which formed off the lower ramp wall of the submerged inlet with increasing angle of attack. The reduction in ram recovery with increasing angle of attack is reflected in the contours of ram-recovery ratio (figs. 12 and 13). These contours show the large increase in areas of low ram recovery in the lower half of the entrance as the angle of attack increased from 0° to 6°. That a flow of the ramp boundary layer into the lower half of the entrance of the submerged inlet may have occurred at an angle of attack is indicated by the curves of pressure coefficient (figs. 26 and 27). These curves show that when the inlet was at an angle of attack the static pressures along the lower edge of the ramp were much lower than those along the center and upper edge of the ramp. The tuft pictures in figure 18 indicate the flow direction along the ramp when the submerged inlet was at 0° and 9° angle of attack.

The contours of ram recovery for the scoop inlet indicate that at 0° angle of attack the losses were mainly along the body side of the entrance (fig. 10) and that at 6° the losses were greater in the lower half of the entrance than in the upper half (fig. 11).

Effect of thickened boundary layer.- Ram-recovery and mass-flow ratios of the two inlets operating with a normal and with a thickened boundary layer are presented in figure 16. Ram-recovery and mass-flow ratio of the submerged inlet were both influenced to a lesser degree by the thickened boundary than were those of the scoop inlet.

Pressure Distribution and Tuft Studies

The plots of pressure distribution show that with similar test conditions the static pressure at the rearmost orifice of the two inlet

[redacted]

models (figs. 21 to 27) tended to recover to about the same value as that of the solid-body model (figs. 19 and 20). This suggests that the inlet installations caused no local separation along the rear section of the afterbody. Peaks of negative pressure coefficient just behind the exterior lip of the entrance were always higher for the scoop inlet than for the submerged inlet at similar test conditions. The formation of peaks of negative pressure coefficient at the inlet lip of a blunt-nosed inlet was shown in reference 6 to result in only a minor increase in drag over that associated with a flat pressure distribution. In general, the curves of pressure coefficient indicate that, for similar test conditions, the measured pressures acting on the fuselage behind the scoop inlet were lower than those on the afterbody of the submerged inlet. However, such lower pressures do not necessarily indicate a higher pressure drag on the scoop afterbody, as there was no curvature of the model afterbody along the surface where the row of orifices was located. (See drawing, fig. 2.)

The tuft studies of the two inlet models at 0° and 9° angles of attack show no indication of separation for either model (figs. 17 and 18).

Drag

All drag measurements with internal flow present were made with the model exit full open (exit ratio of 1.00) and the inlet rake removed. The curves in figures 6 and 7 show values of mass-flow ratio with the inlet rake installed. It is probable that the mass-flow ratios during drag measurements (inlet rake removed) were somewhat higher than those indicated in figures 6 and 7 for an exit ratio of 1.00, but about equal through the two inlets for similar values of Mach number and angle of attack.

Total drag.- The curves in figure 28 indicate that there was no consistent difference between the total-drag coefficient of the scoop-inlet model and that of the submerged-inlet model except at 6° angle of attack where the coefficient of total drag for the scoop-inlet model was always the higher.

Figure 30 indicates that, for zero mass-flow ratio and 0° angle of attack, the total-drag coefficient with the scoop inlet was greater than with the submerged inlet for Mach numbers above approximately 0.93. The increase in total-drag coefficient of the solid body due to angle of attack and to a thickened boundary layer is shown in figure 29.

Increment of external drag.- The curves of figure 32 indicate that, at 0° and 6° angles of attack, the increment of external drag due to the

scoop inlet was always greater than that due to the submerged inlet, except for Mach numbers above 1.08 at 0°. The coefficient of internal drag, used in the calculation of the increment of external drag, was always lower for the scoop inlet than for the submerged inlet (fig. 31).

CONCLUSIONS

From an investigation within a Mach number range of 0.79 to 1.12, an angle-of-attack range of 0° to 9°, and a mass-flow ratio range of 0 to 0.92, the following conclusions were reached:

1. At mass-flow ratios below approximately 0.50, the ram-recovery ratio measured at the entrance of an NACA submerged inlet was higher than for a scoop inlet (without boundary-layer control) at all angles of attack and Mach numbers of this test. At the maximum mass-flow ratios and 0° angle of attack recovery of the two inlets was about equal.

2. Increasing the angle of attack had a more adverse effect on the ram recovery of the submerged inlet than on that of the scoop inlet. Such adverse effect on the submerged inlet appeared at lower angles of attack as Mach number increased.

3. The increment of external drag was greater for the scoop inlet than for the submerged inlet up to a Mach number of 1.08 at 0° angle of attack and up to the maximum Mach number of 1.10 at 6°.

Ames Aeronautical Laboratory,
National Advisory Committee for Aeronautics,
Moffett Field, Calif.

REFERENCES

1. Axelson, John A., and Taylor, Robert A.: Preliminary Investigation of the Transonic Characteristics of an NACA Submerged Inlet. NACA RM A50C13, 1950.

2. Selna, James: Preliminary Investigation of a Submerged Inlet and a Nose Inlet in the Transonic Flight Range With Free-Fall Models. NACA RM A51B14, 1951.

[redacted]

3. Hall, Charles F., and Barclay, F. Dorn: An Experimental Investigation of NACA Submerged Inlets at High Subsonic Speeds. I - Inlets Forward of the Wing Leading Edge. NACA RM A8B16, 1948.

4. Chang, Chien-Chien: A Simplified Method of Obtaining Drag of a High-Speed Body from Wake Surveys. Jour. Aero. Sci., vol. 15, no. 2, Feb. 1948, pp. 123-127.

5. Mossman, Emmet A.: Summary of Information on Air Inlets. NACA Conference on Aerodynamic Problems of Transonic Airplane Design. A Compilation of Papers Presented at Langley Aeronautical Laboratory, September 27-29, 1949, pp. 367-379.

6. Pendley, Robert E., and Smith, Norman F.: An Investigation of the Characteristics of Three NACA I-Series Nose Inlets at Subcritical and Supercritical Mach Numbers. NACA RM L8L06, 1949.

(a) Solid body.

(b) Body with scoop inlet.

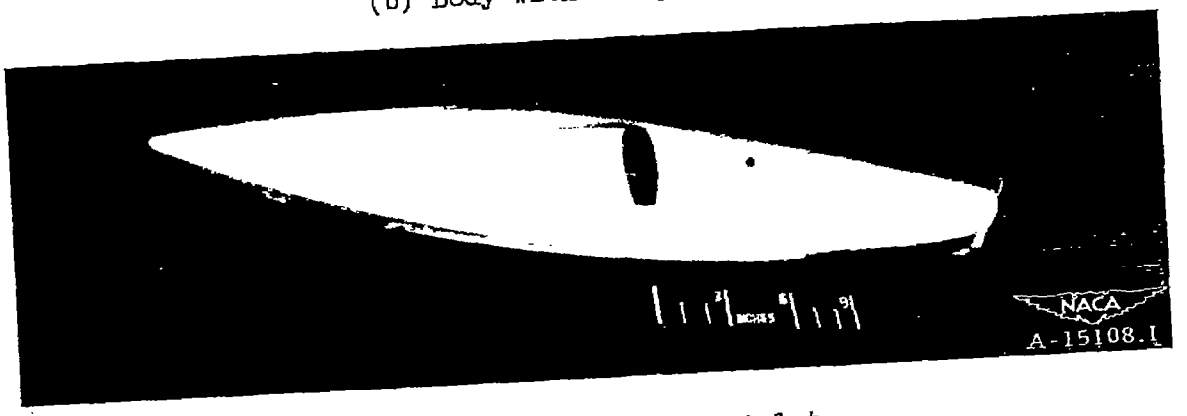

(c) Body with submerged inlet.

Figure 1.- Models mounted on transonic bump.

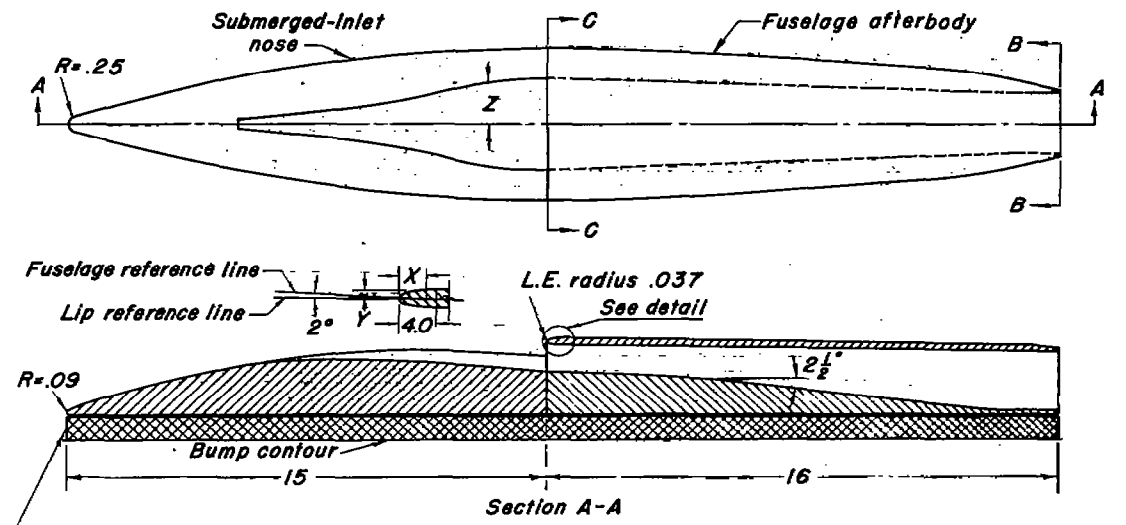

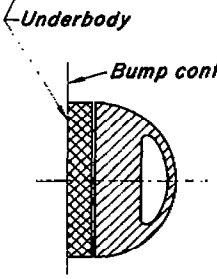

Ramp floor coordinates

Fus. sta.	Ord.
5.25	1.52
6.00	1.63
7.00	1.73
8.00	1.77
9.00	1.77
10.00	1.75
11.00	1.71
12.00	1.67
13.00	1.58
14.00	1.50
15.00	1.40

Ramp wall coordinates

Fus. sta.	Z
5.250	.127
6.225	.239
7.200	.352
8.175	.464
9.150	.586
10.125	.726
11.100	.910
12.075	1.149
13.050	1.374
14.025	1.491
15	1.500

Lip coordinates

X	±Y
0	0
.05	.047
.10	.064
.15	.076
.20	.084
.25	.089
.30	.092
.35	.093
.40	.094

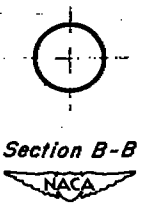

Note: All dimensions are in inches unless otherwise specified.

Figure 2.—Dimensions of fuselage afterbody and submerged inlet.

[redacted]

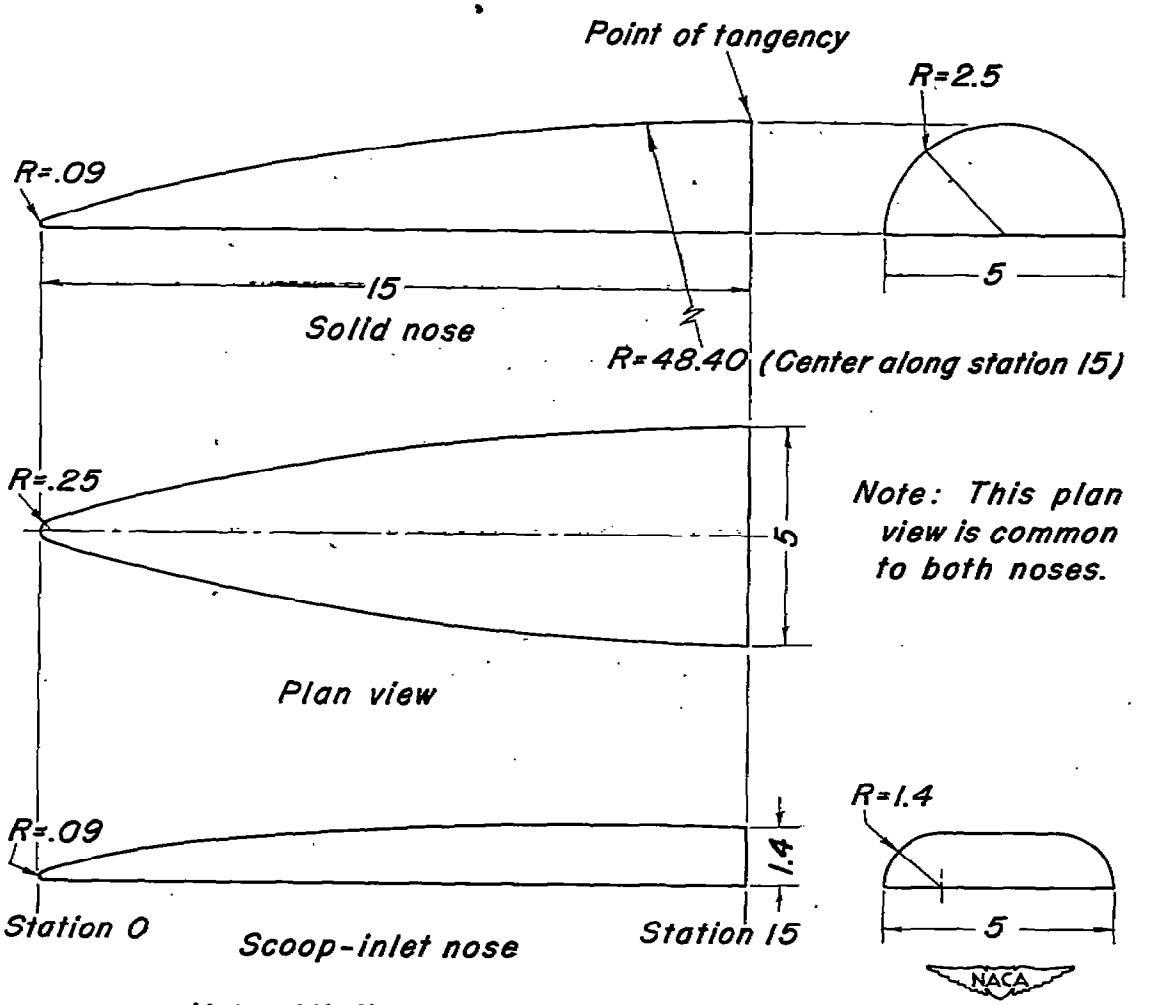

Figure 3.—Dimensions of solid nose and scoop inlet.

[redacted]

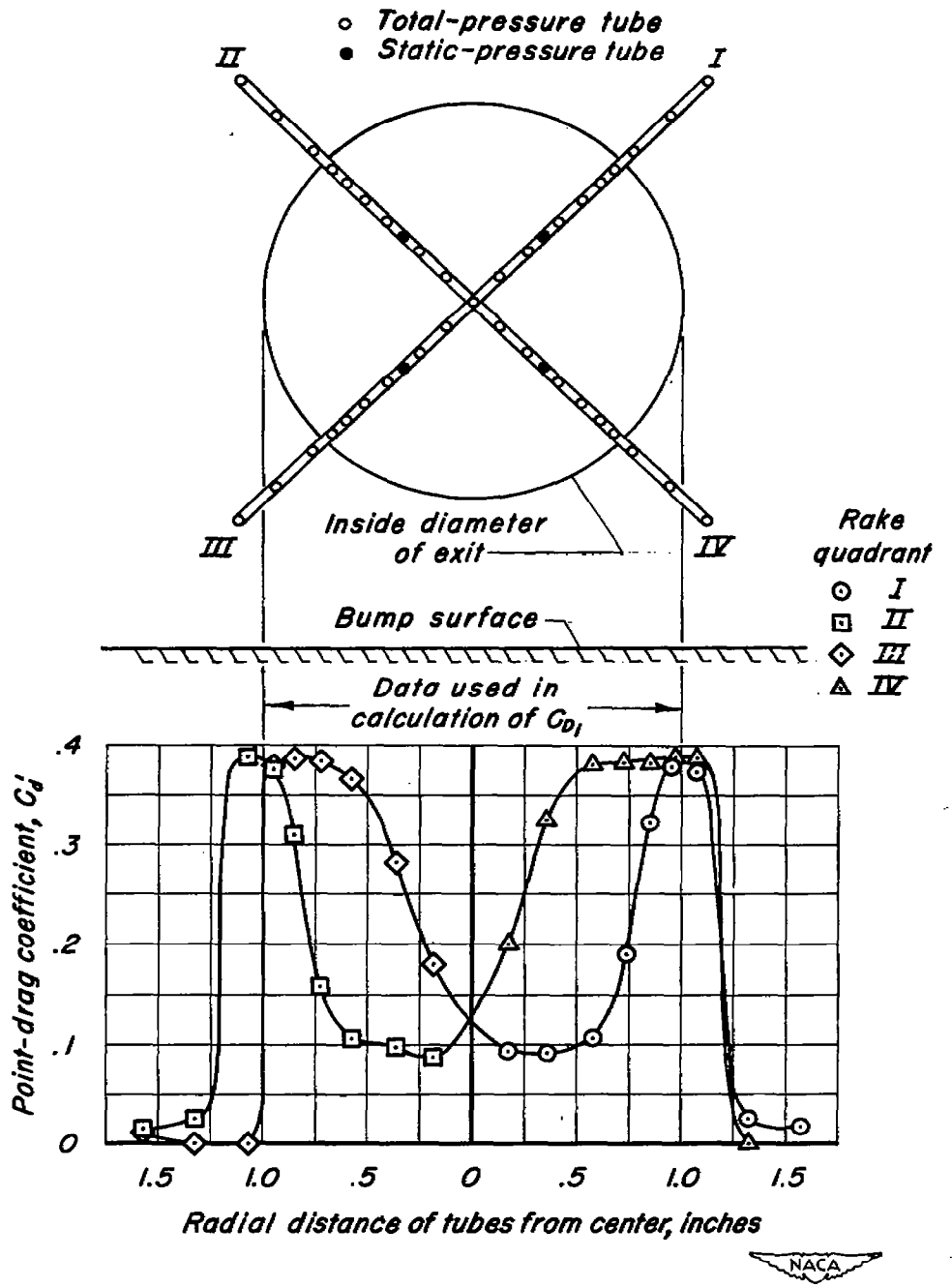

Figure 4.–Location of exit-rake tubes and a typical plot of point-drag coefficient at the exit for the scoop-inlet model. M_o, 1.00; α, 0°; $\frac{m_i}{m_o} = 0.88$.

[redacted]

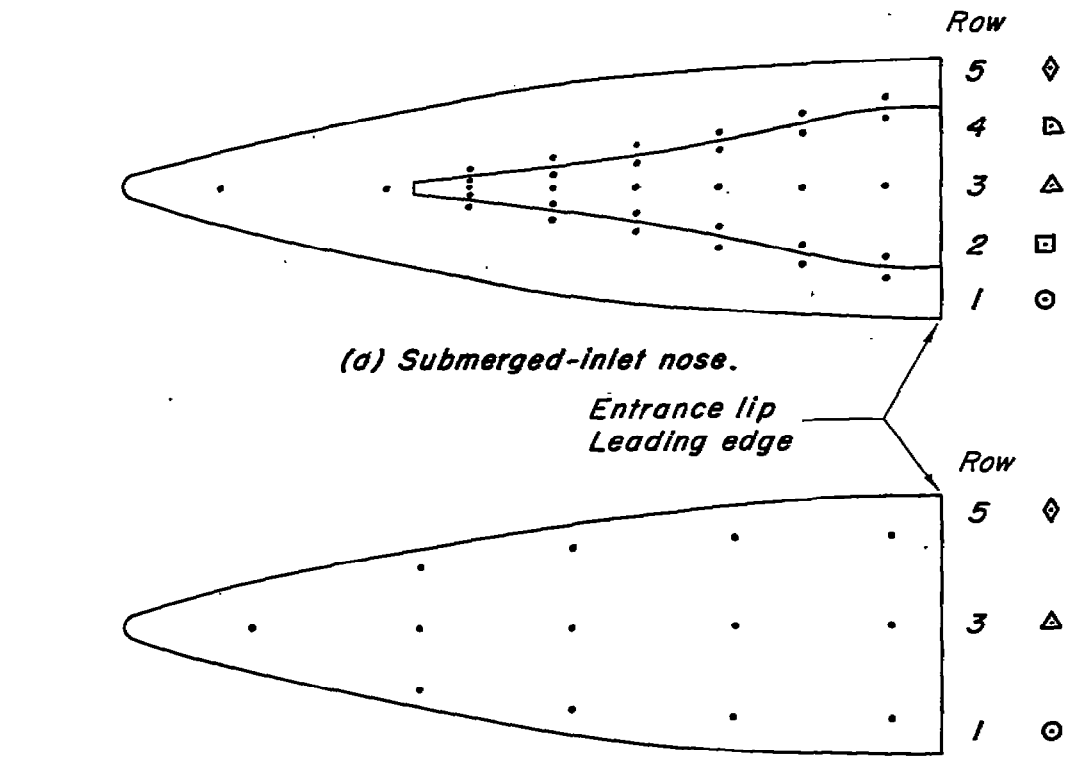

(a) Submerged-inlet nose.

(b) Solid and scoop-inlet nose.

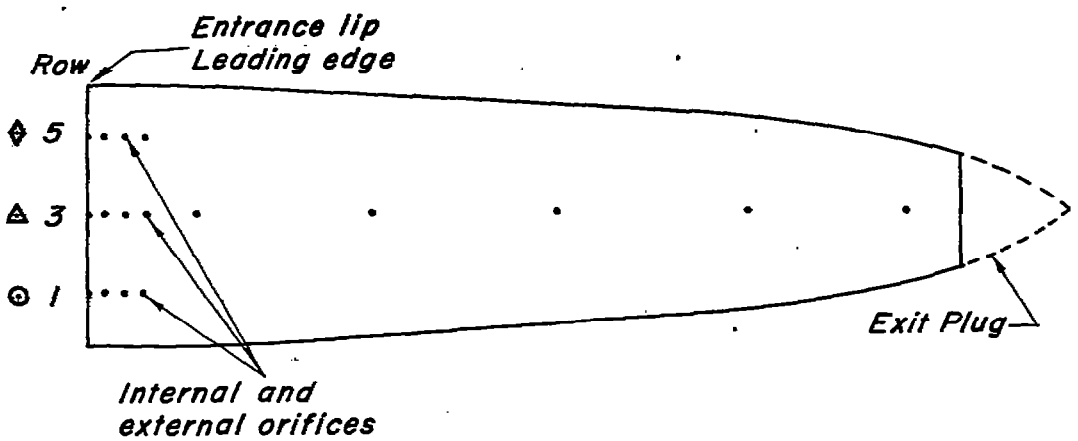

(c) Fuselage afterbody.

Figure 5.–Location of rows of pressure orifices along the body.

[redacted] *

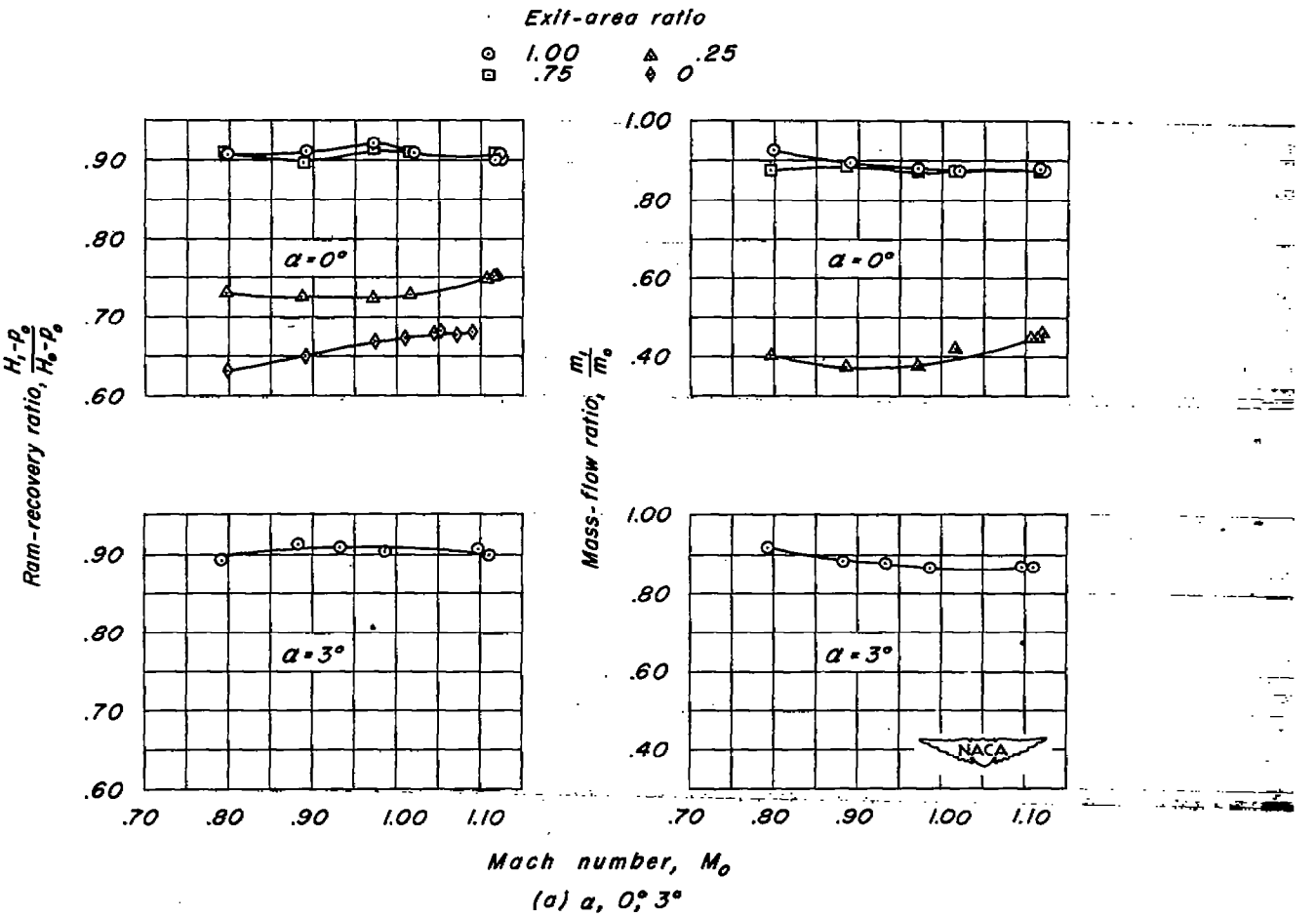

(a) a, 0°, 3°

Figure 6.—Variation of ram-recovery ratio and mass-flow ratio at the entrance of the scoop inlet at four angles of attack.

[redacted]

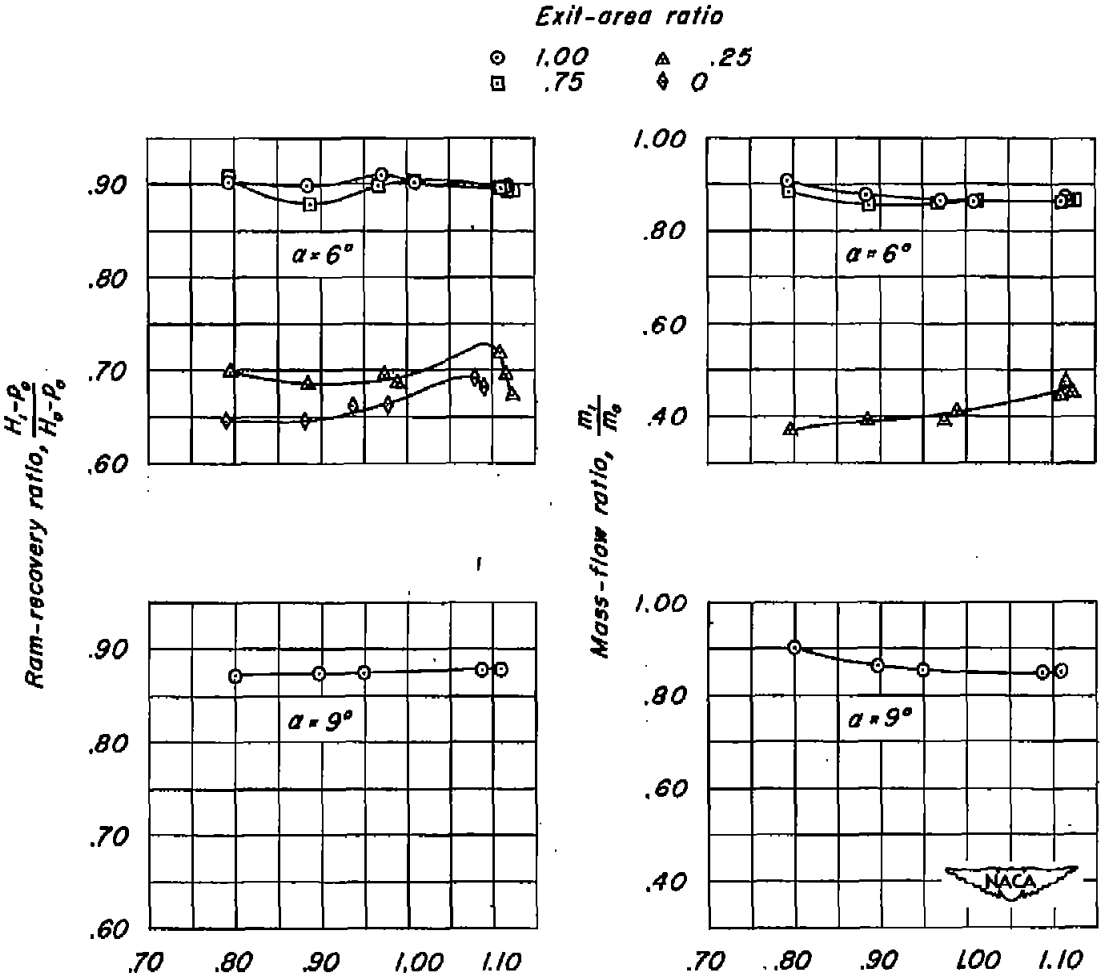

(b) α, 6°, 9°

Figure 6.—Concluded.

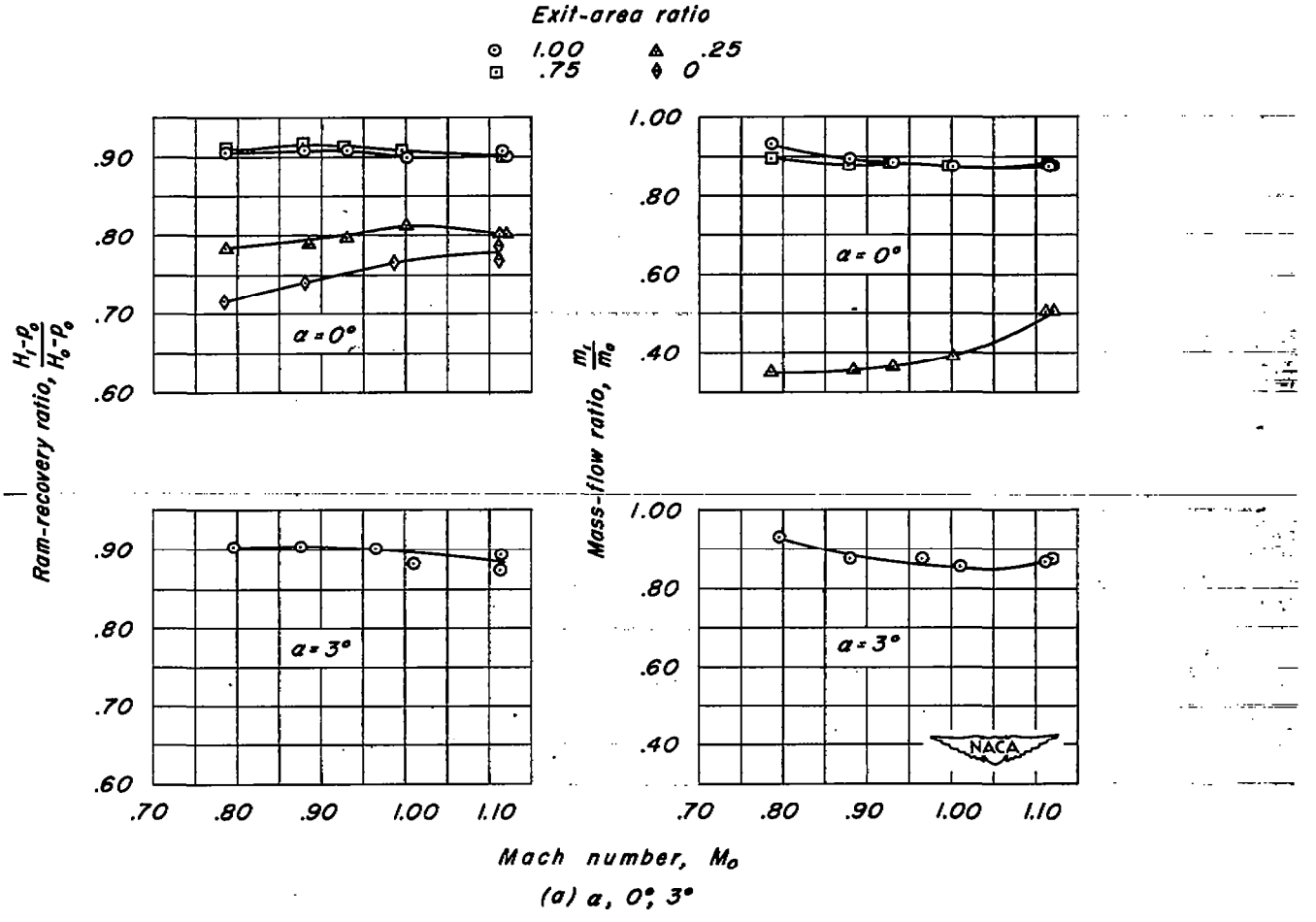

(a) α, 0°; 3°

Figure 7.—Variation of ram-recovery ratio and mass-flow ratio at the entrance of the submerged inlet at four angles of attack.

[redacted]

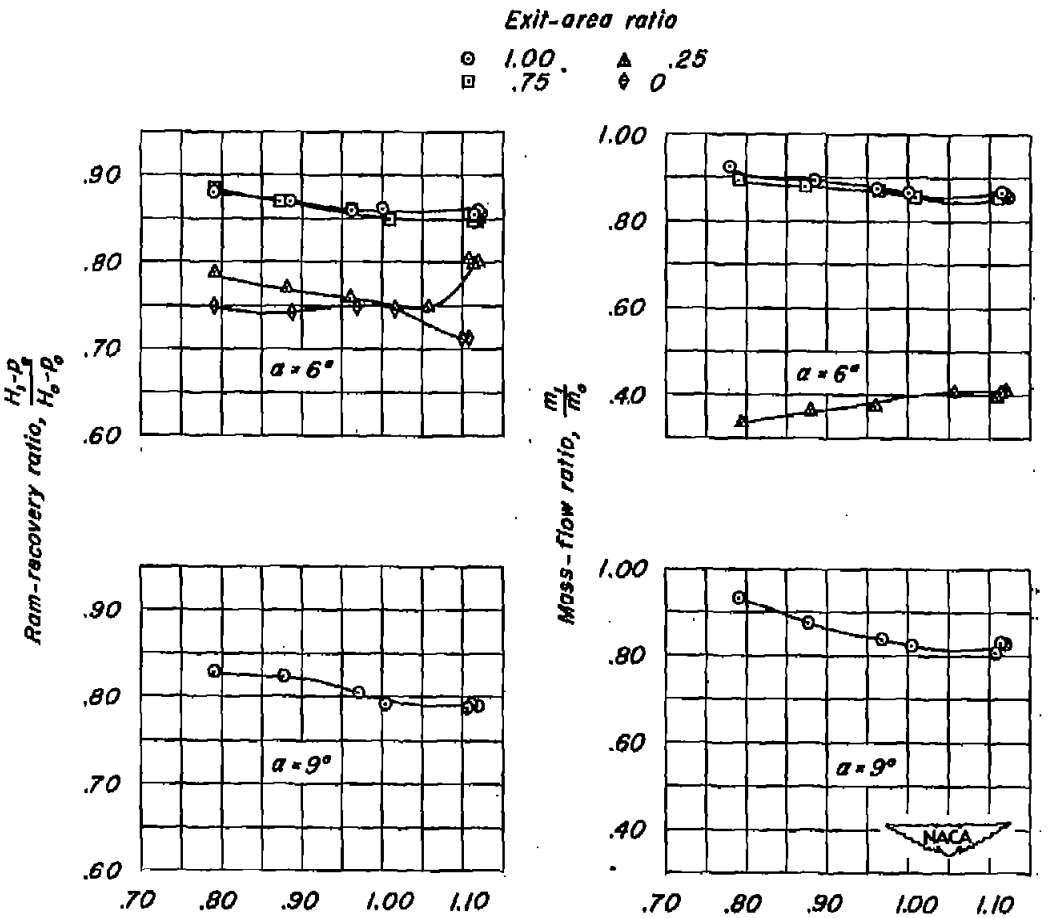

(b) α, 6°, 9°

Figure 7.—Concluded.

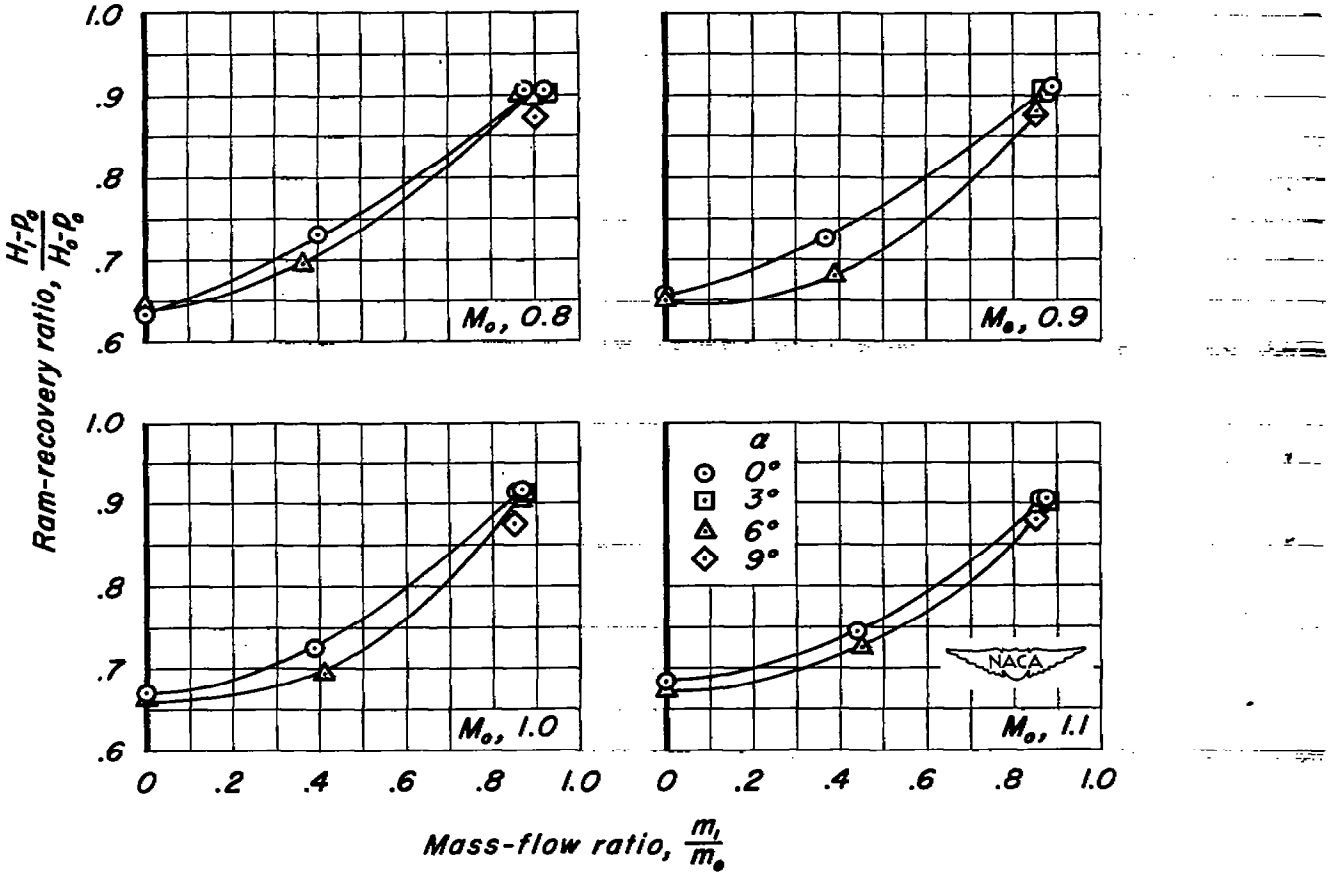

Figure 8.—Variation of ram-recovery ratio with mass-flow ratio at the entrance of the scoop inlet at four angles of attack and four Mach numbers.

[redacted]

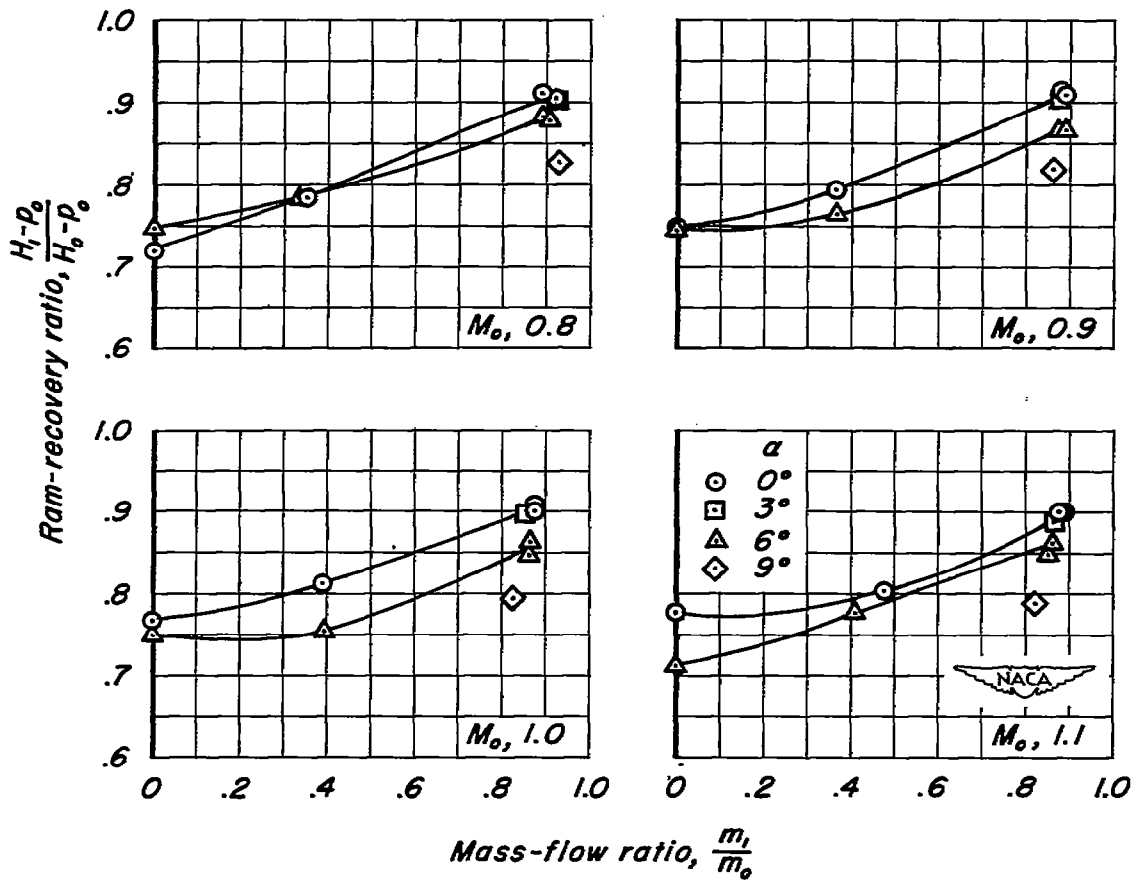

Figure 9.—Variation of ram-recovery ratio with mass-flow ratio at the entrance of the submerged inlet at four angles of attack and four Mach numbers.

[redacted]

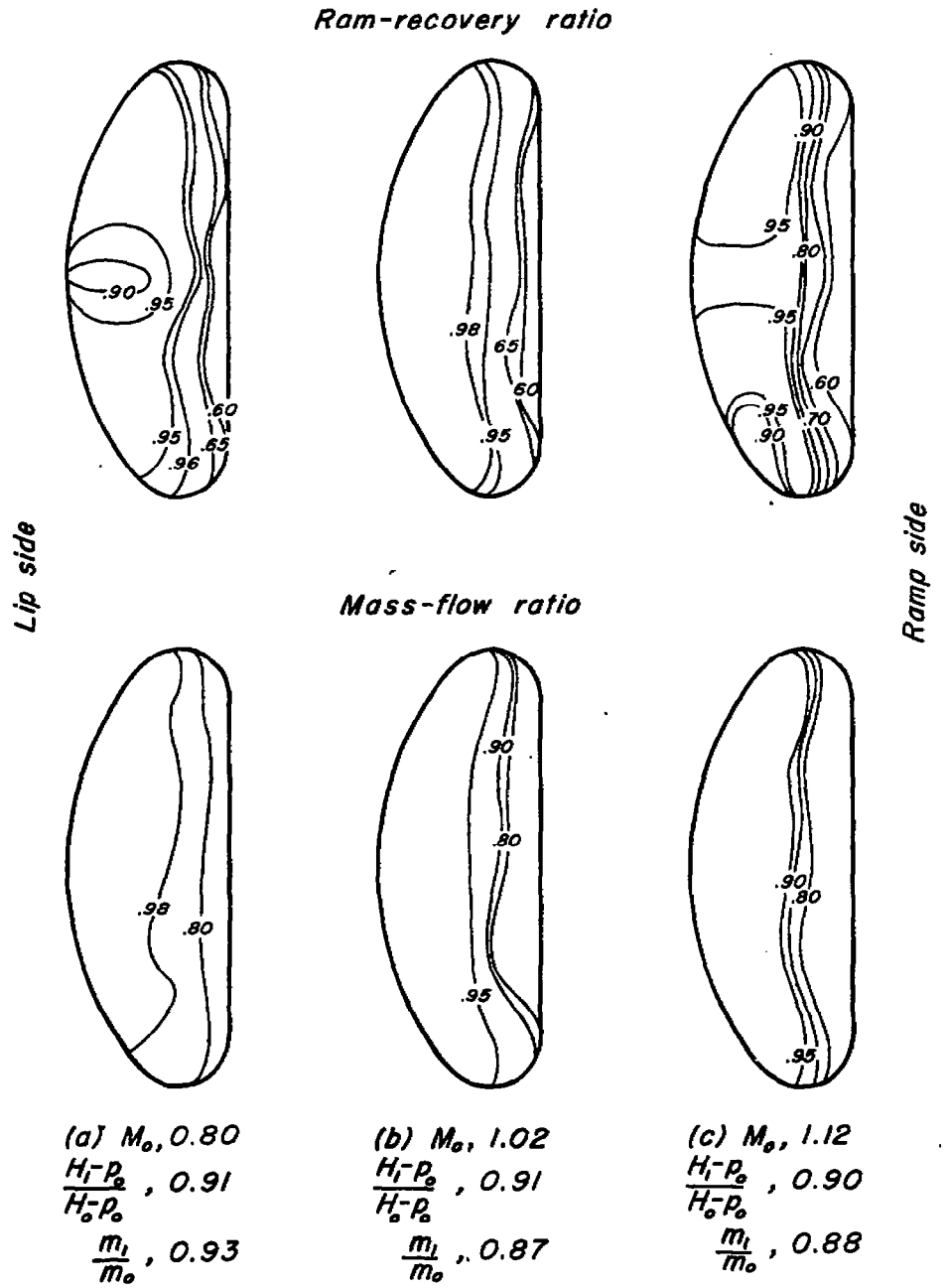

Figure 10.–Ram-recovery and mass-flow contours at the entrance of the scoop inlet; α, 0°

[redacted]

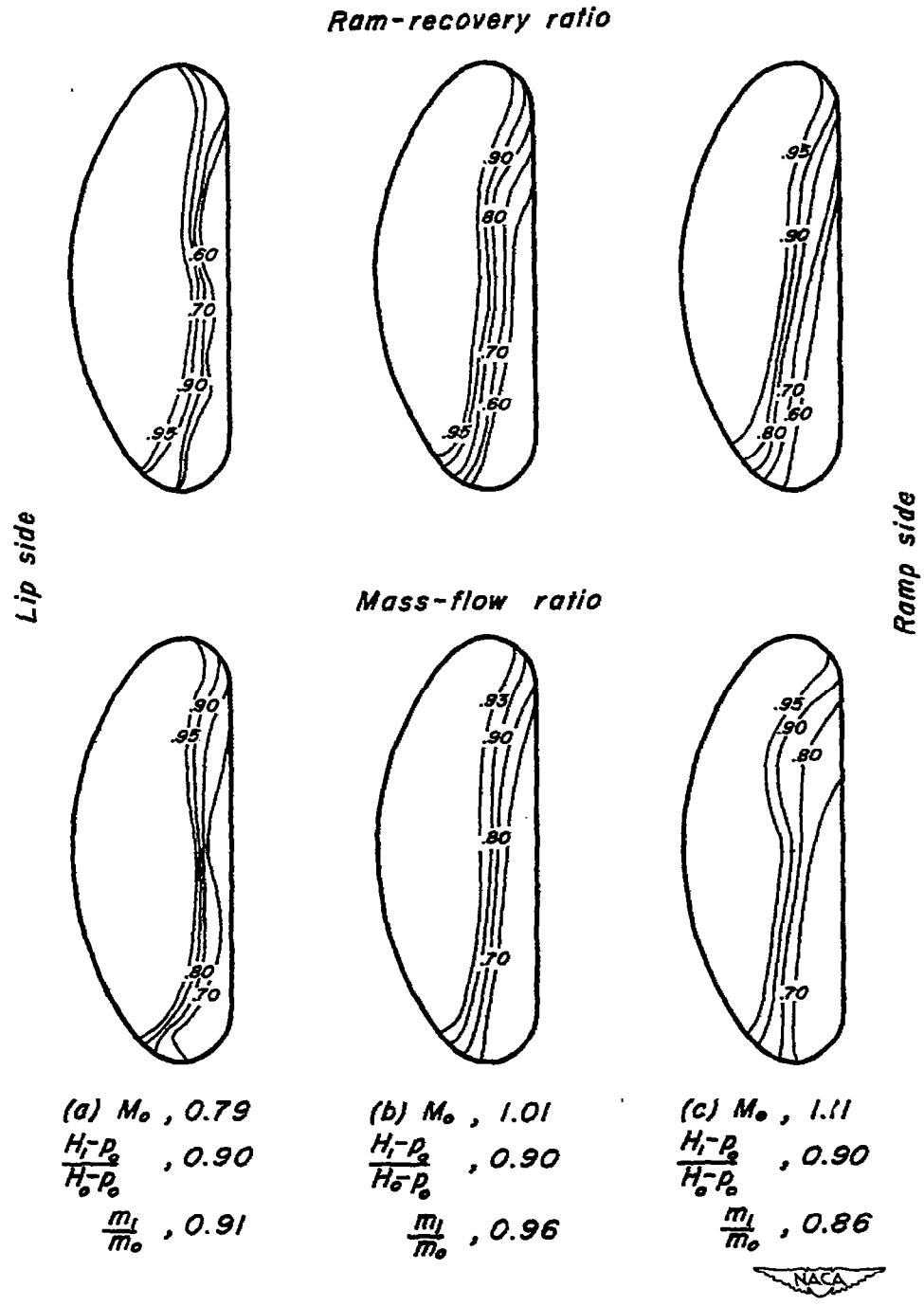

Figure 11.–Ram-recovery and mass-flow contours at the entrance of the scoop inlet; α, 6°

[redacted]

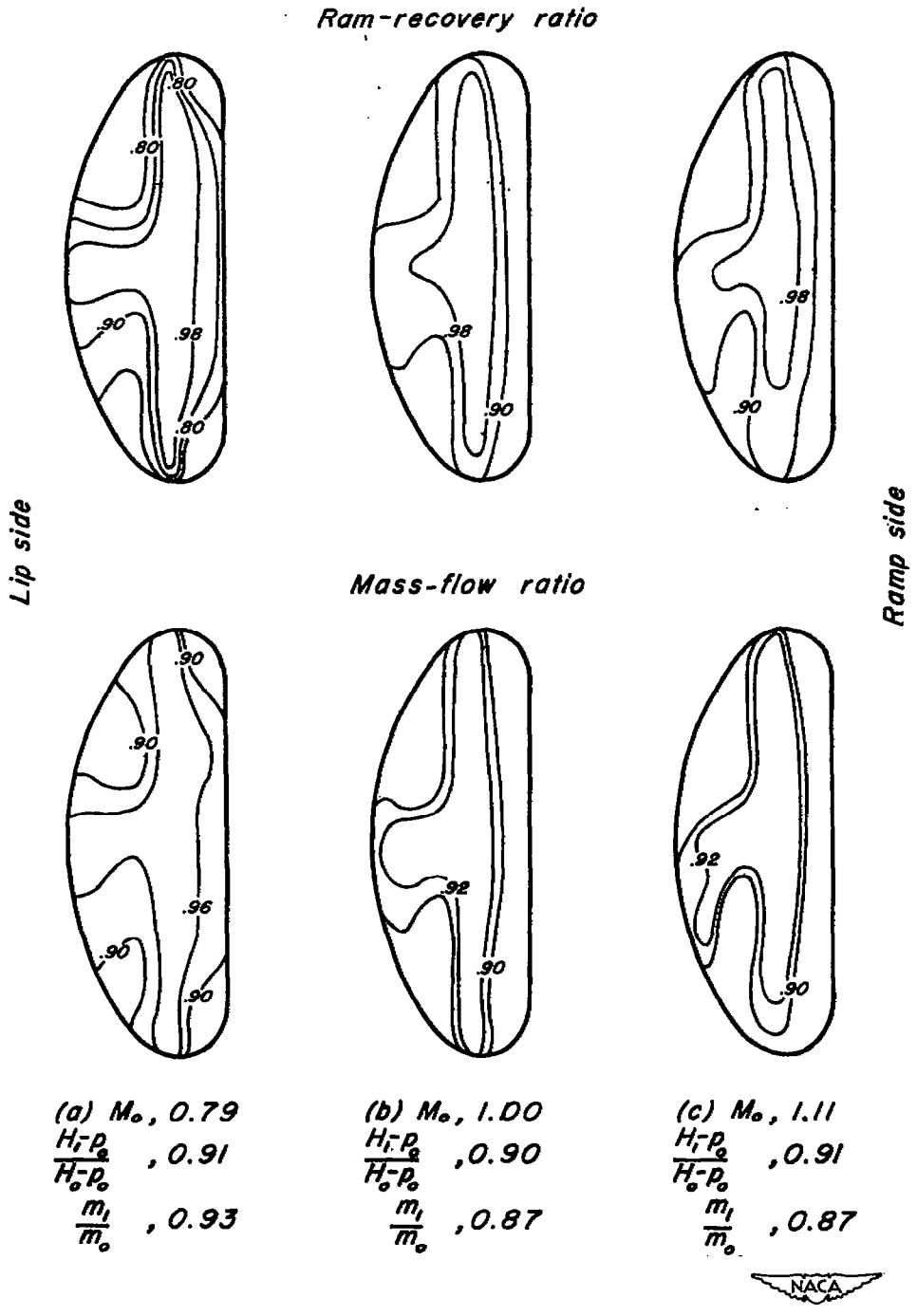

Figure 12.–Ram-recovery and mass-flow contours at the entrance of the submerged inlet; a, 0°

[redacted]

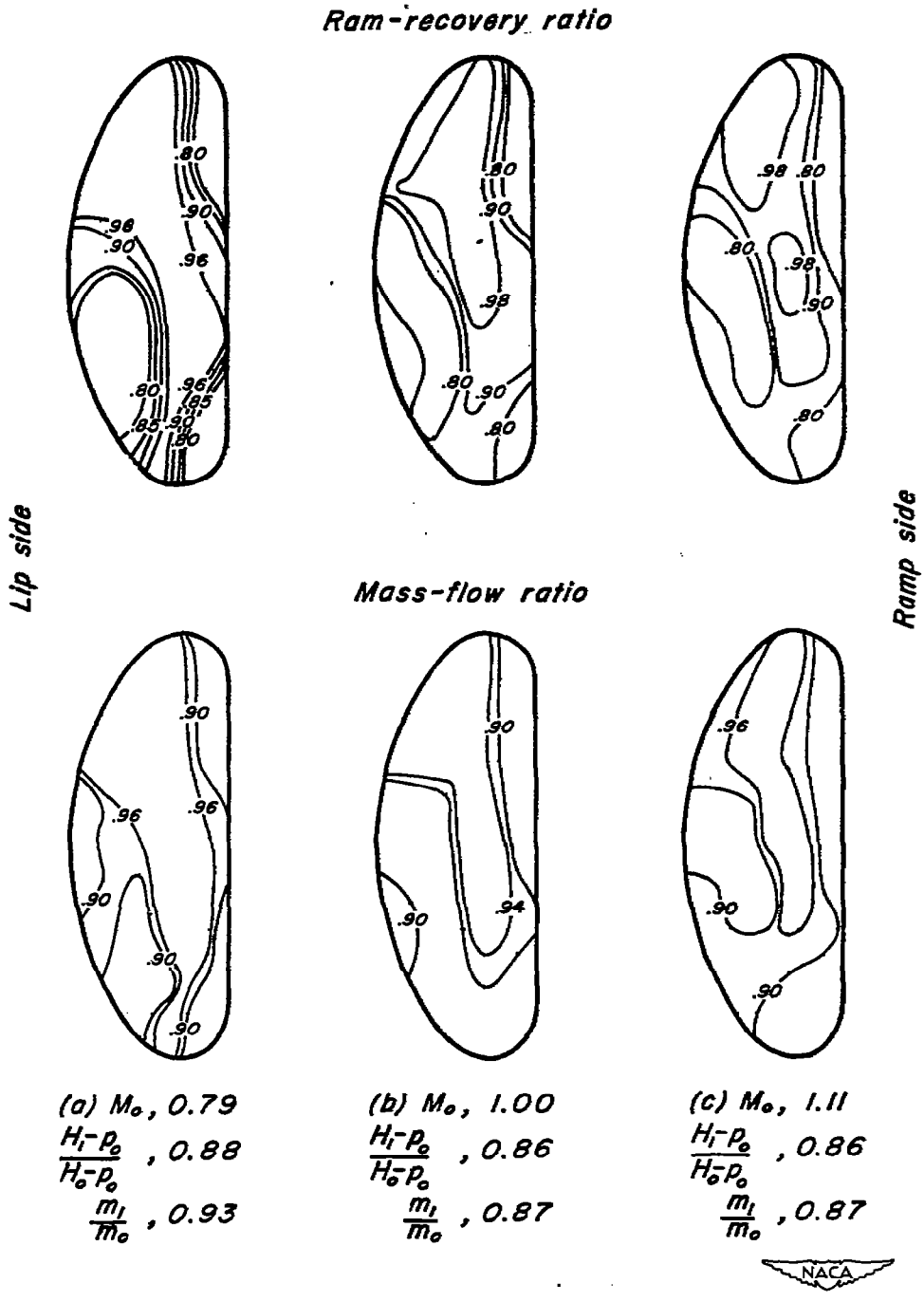

Figure 13.–Ram-recovery and mass-flow contours at the entrance of the submerged inlet; α, 6°.

[redacted]

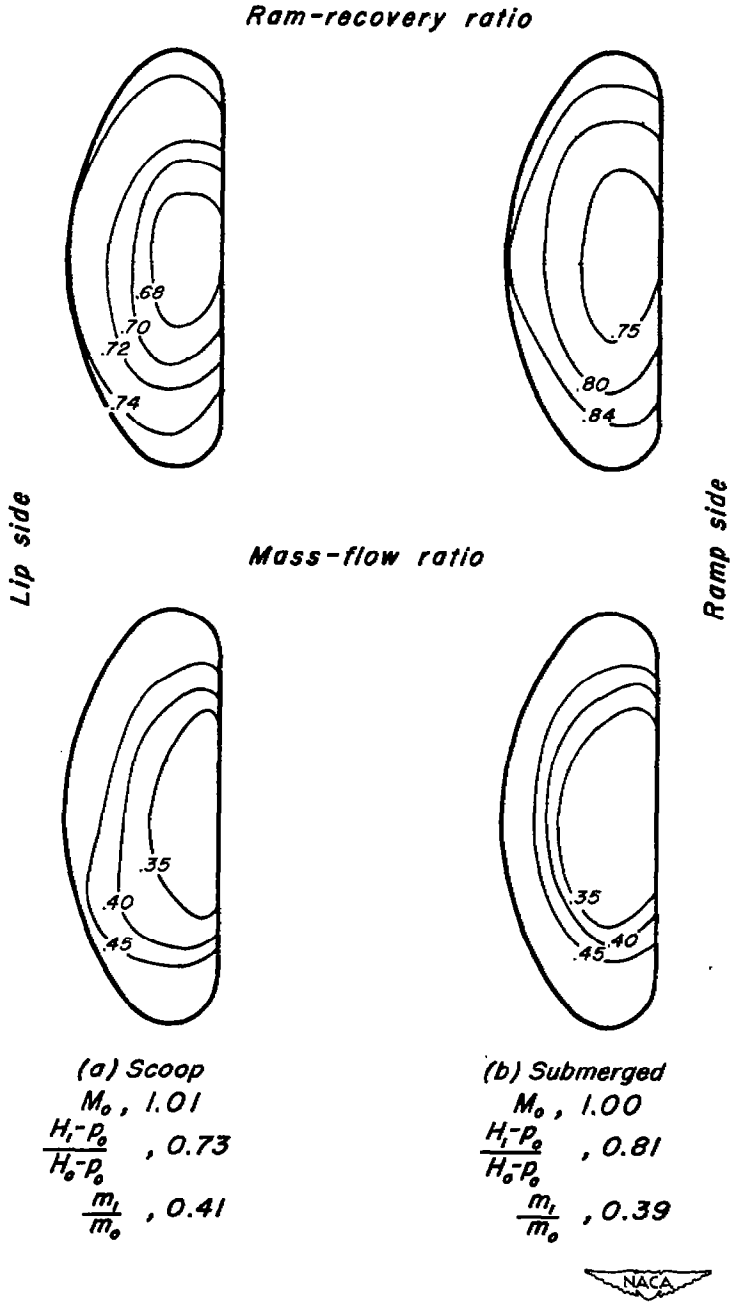

Figure 14.-Ram-recovery and mass-flow contours at the entrance of the scoop and the submerged inlets. Low mass-flow ratio; α, 0°.

[redacted]

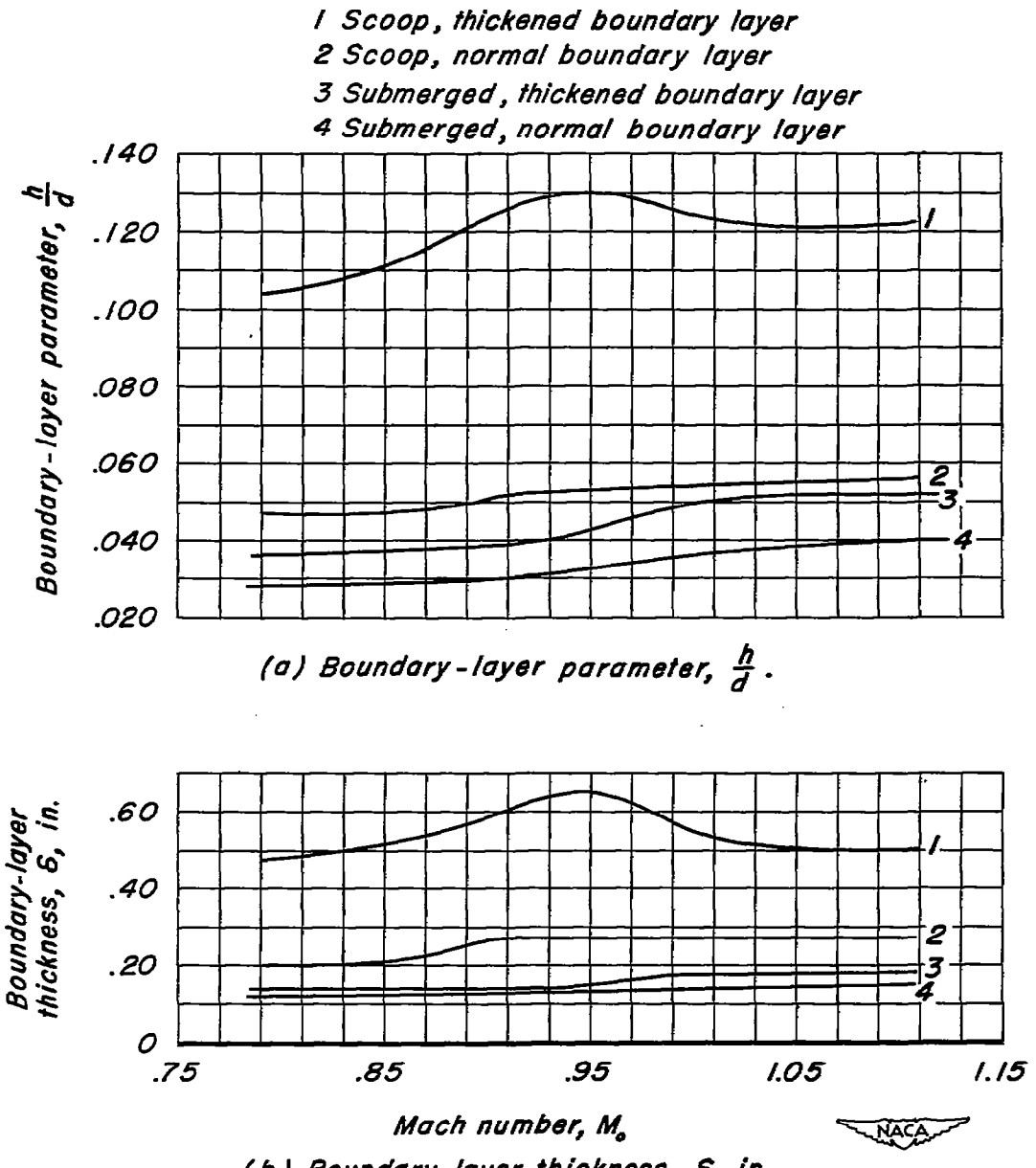

Figure 15.—Variation of boundary-layer parameter and boundary-layer thickness with Mach number $\frac{1}{8}$ inch in front of the entrance of the scoop inlet and the submerged inlet with a normal and a thickened boundary layer; $\frac{m_i}{m_e} = 0.88$, a, 0.°

[redacted]

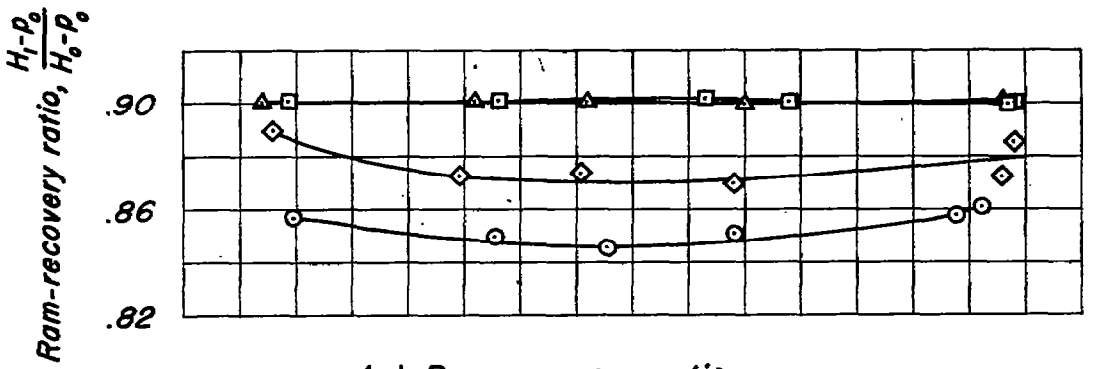

(a) Ram-recovery ratio.

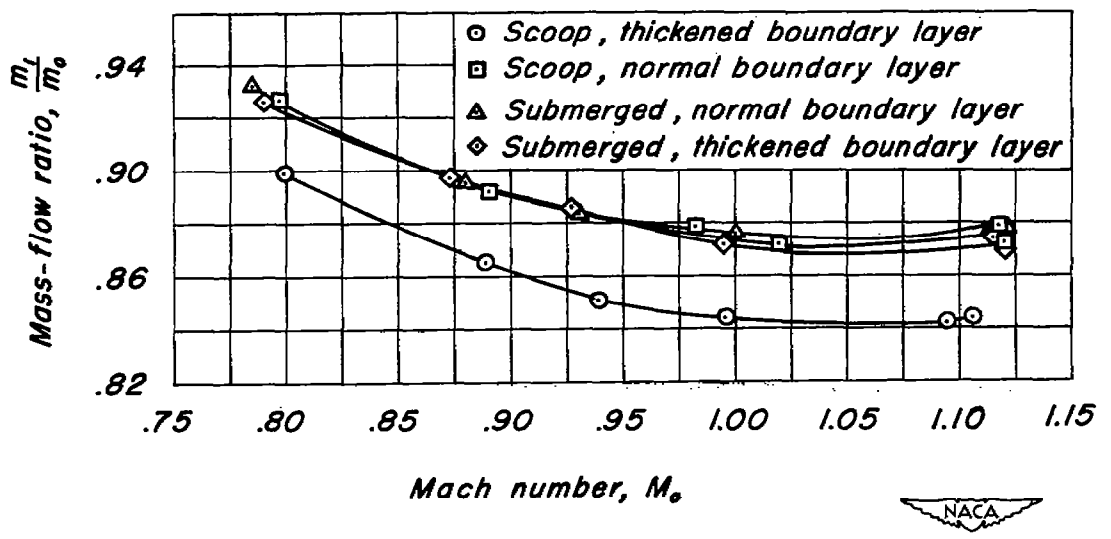

(b) Mass-flow ratio.

Figure 16.–Variation of ram-recovery ratio and mass-flow ratio with Mach number at the entrance of the scoop inlet and the submerged inlet with a normal and a thickened boundary layer; α, 0°.

[redacted]

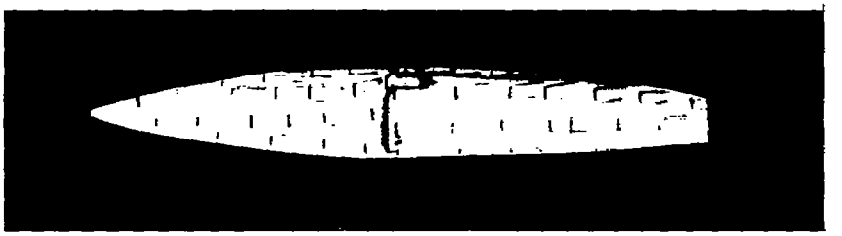

M_o, 0.87

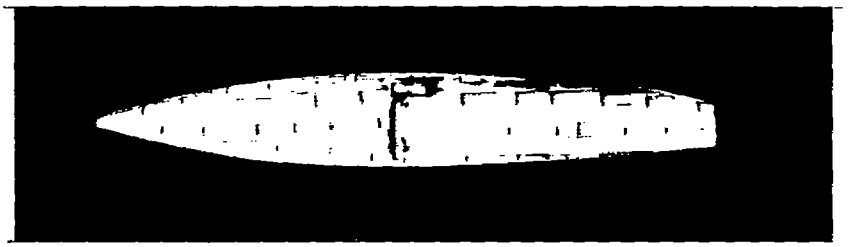

M_o, 1.09

(a) α, 0°

M_o, .85

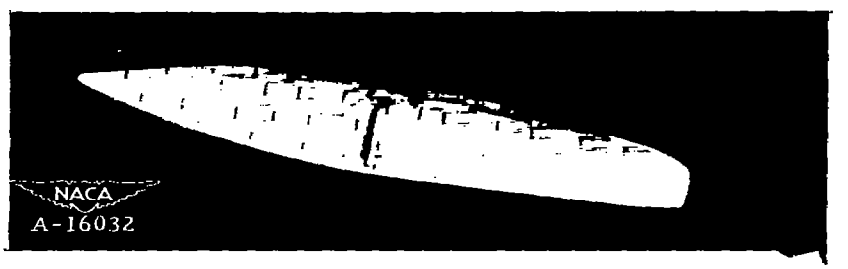

M_o, 1.11

(b) α, 9°

Figure 17.- Tufts on body with scoop inlet.

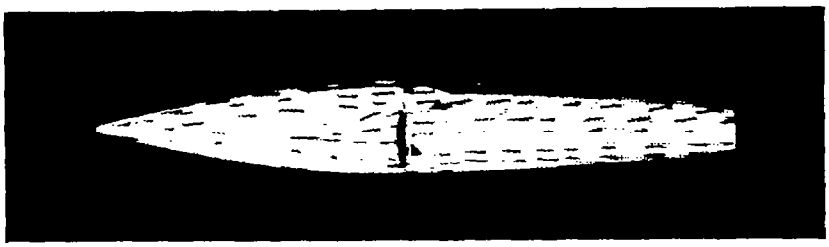

M_o, 0.88

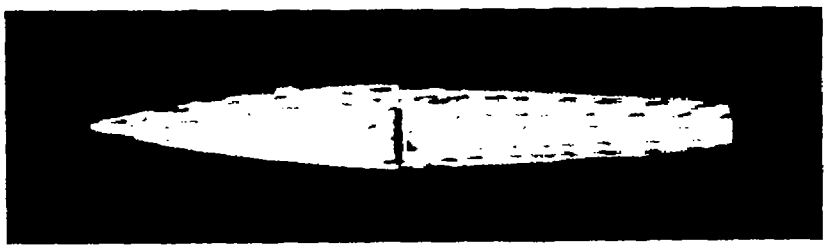

M_o, 1.12

(a) α, 0°

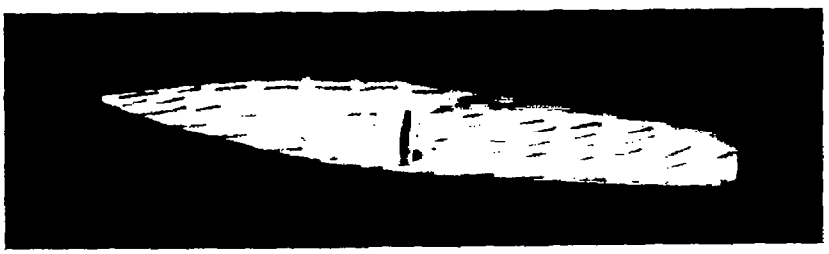

M_o, 0.80

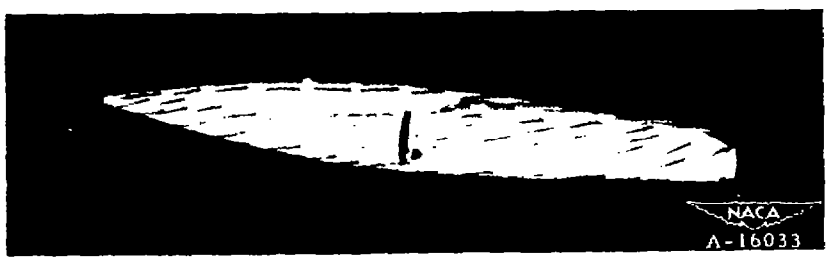

M_o, 1.12

(b) α, 9°

Figure 18.- Tufts on body with submerged inlet.

[redacted]

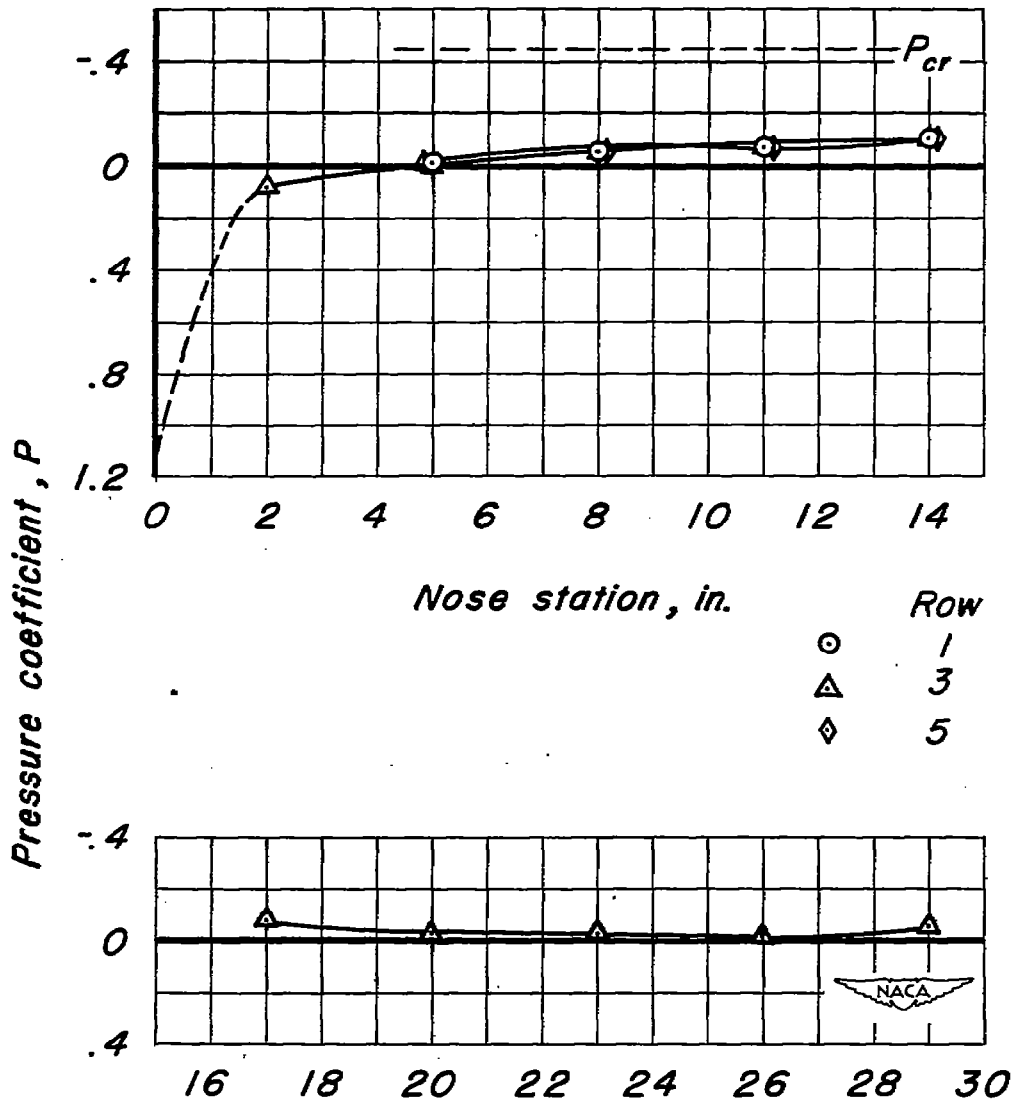

(a) M_o, 0.79

Figure 19.—Pressure distribution along the solid body with exit cone; α, 0°

[redacted]

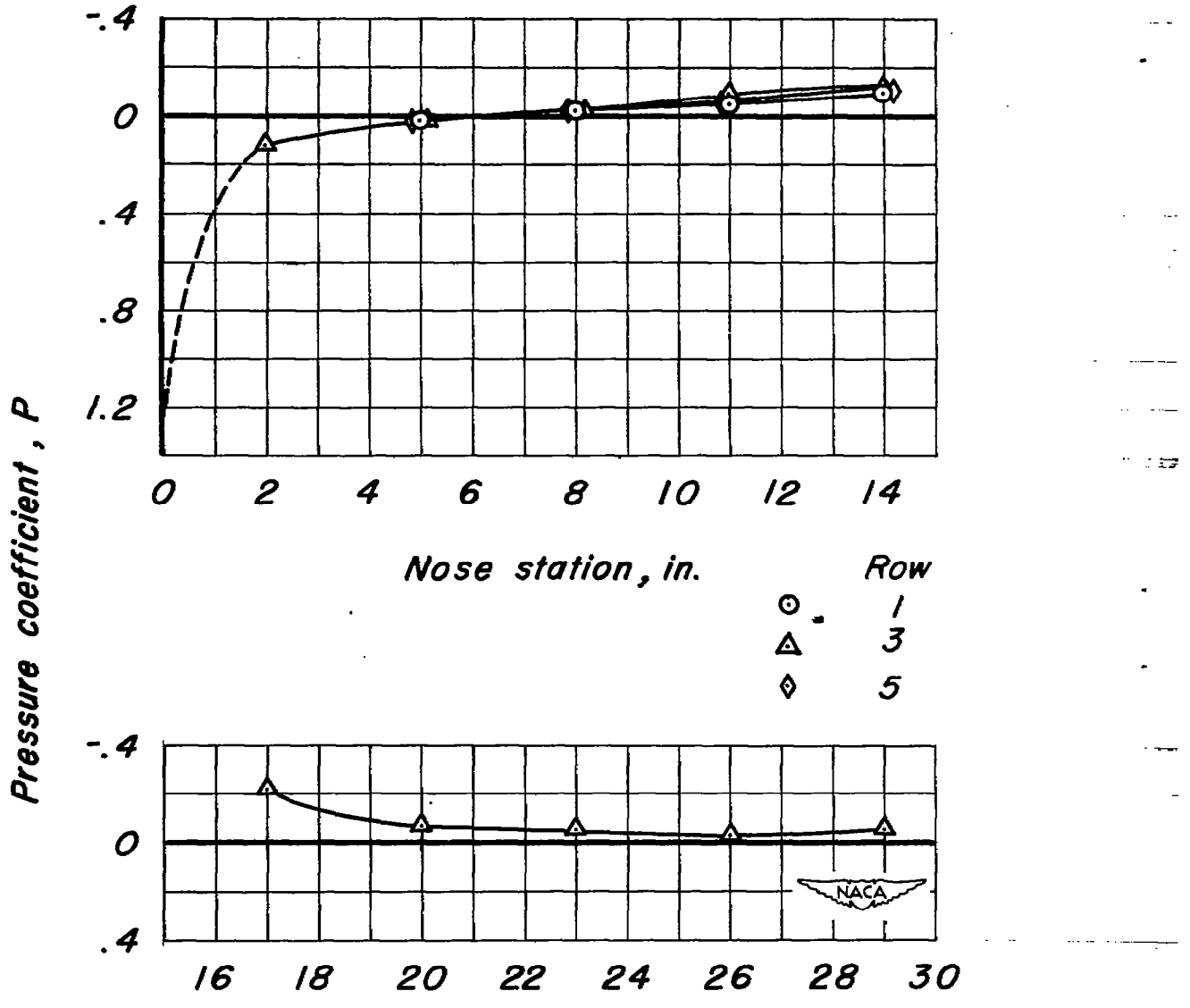

(b) M_o, 1.01

Figure 19.—Continued.

[redacted]

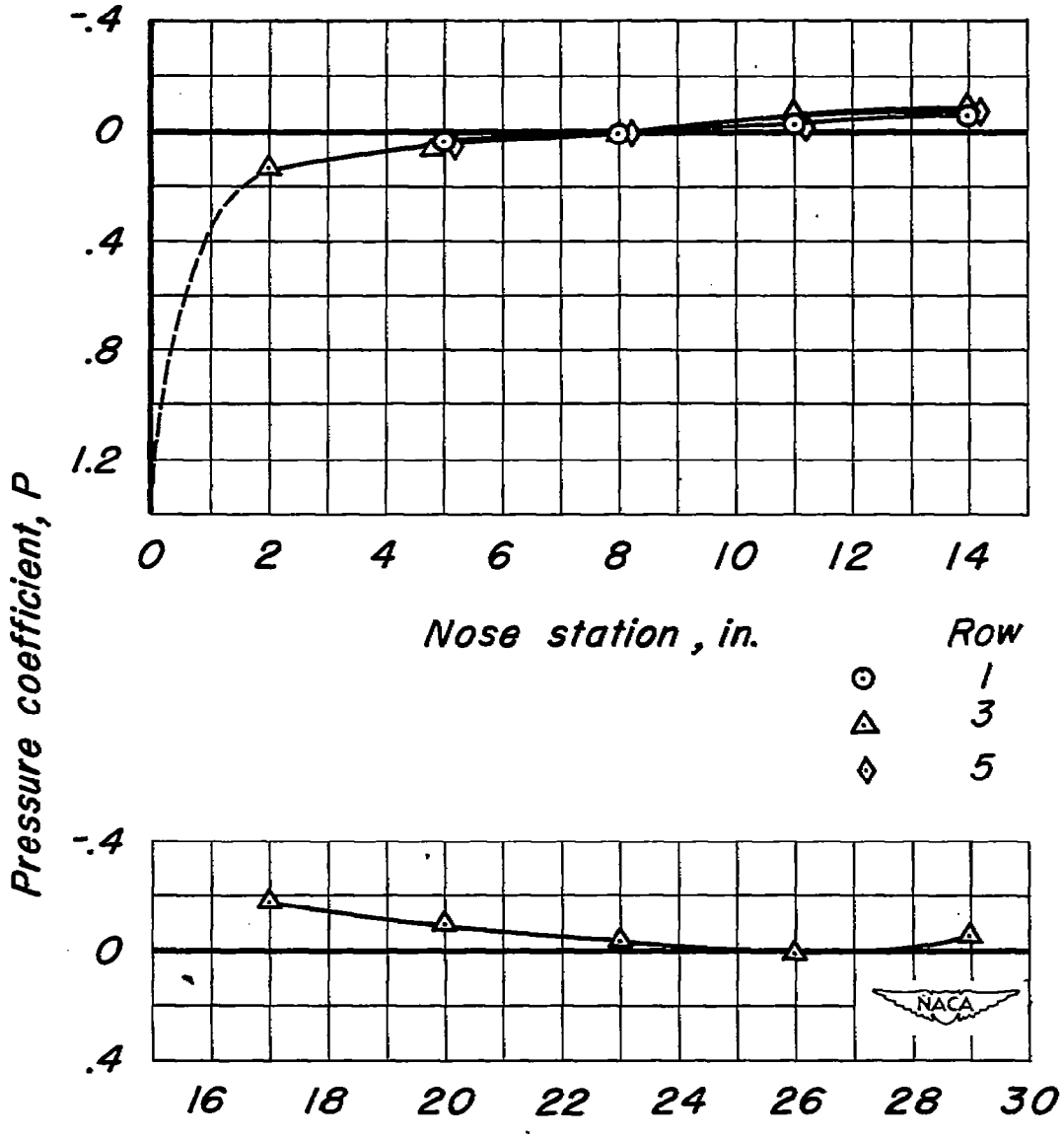

(c) M_o, 1.12

Figure 19.—Concluded.

[redacted]

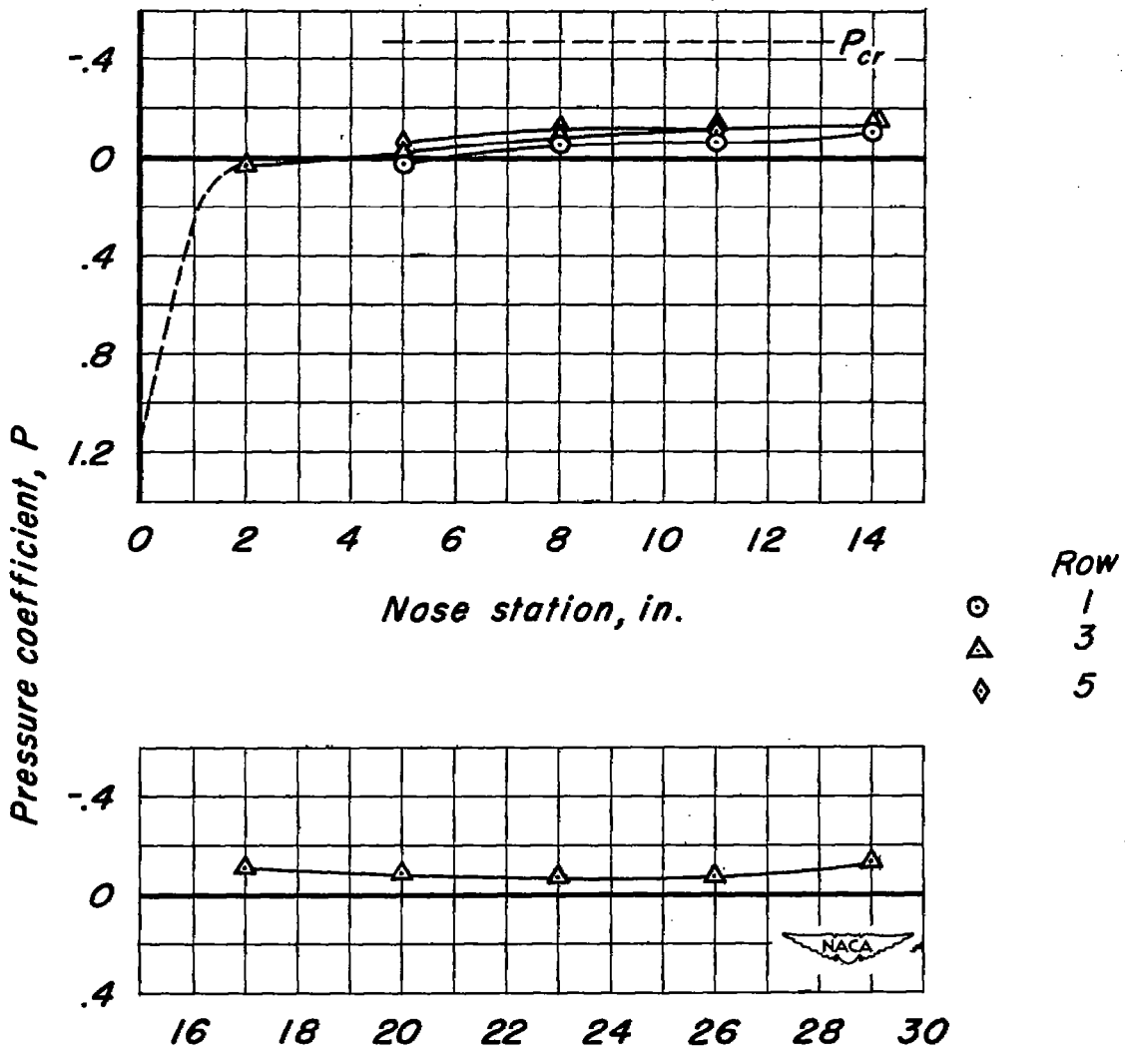

(a) M_o, 0.79

Figure 20.—Pressure distribution along the solid body with exit cone; α, 6°

[redacted]

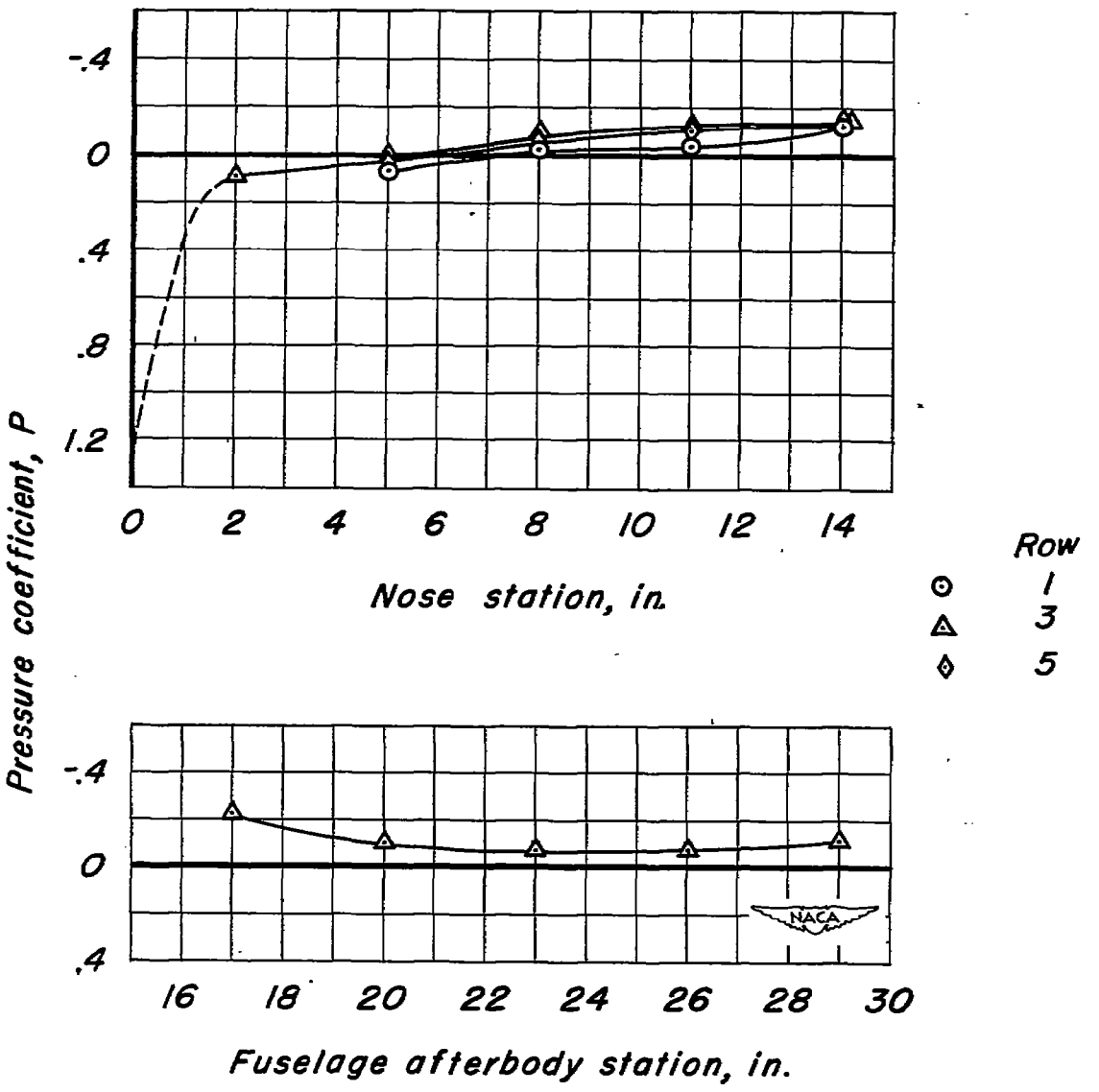

(b) M_o, 1.01

Figure 20.—Continued.

[redacted]

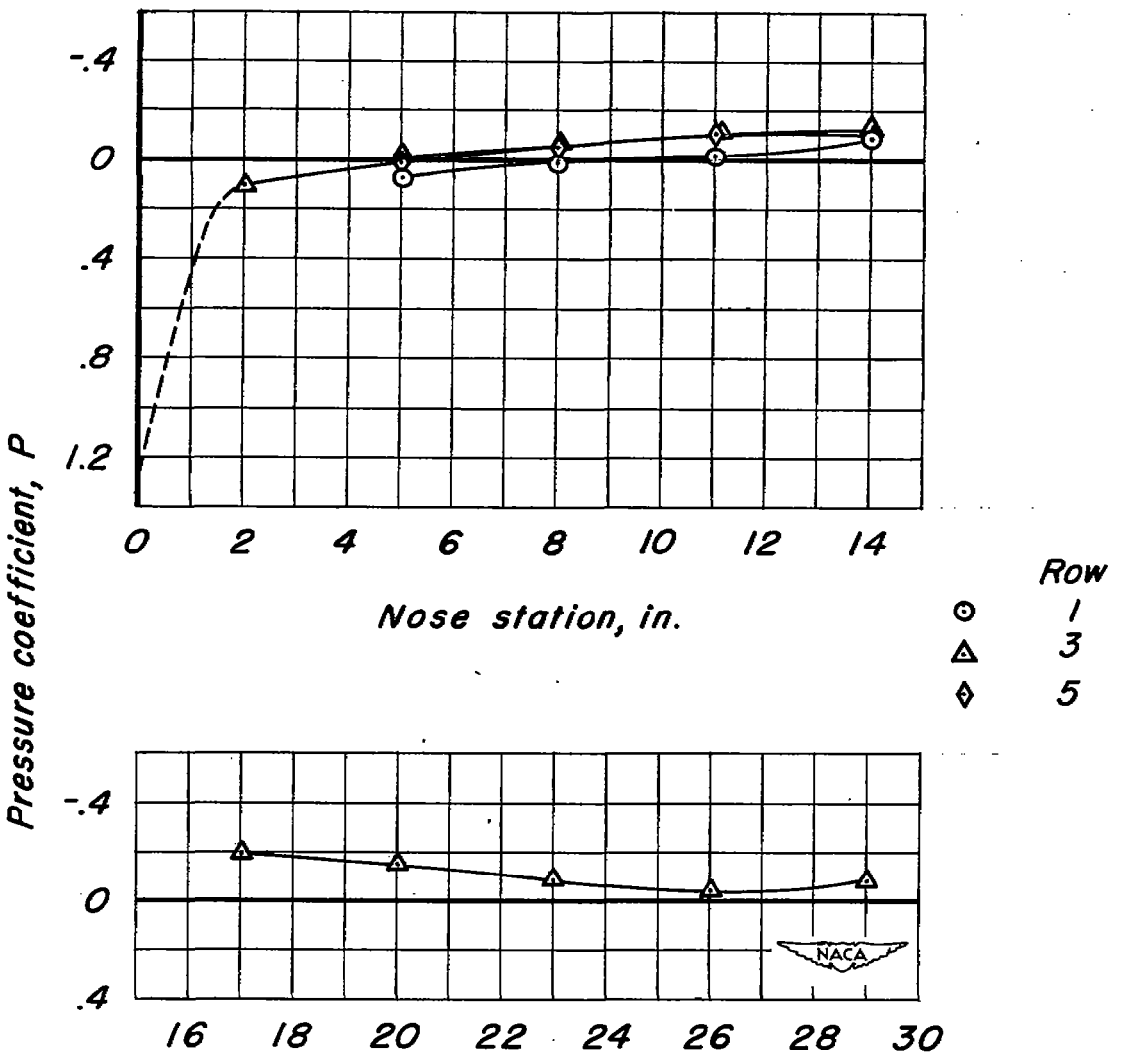

(c) M_o, 1.11

Figure 20.—Concluded.

[redacted]

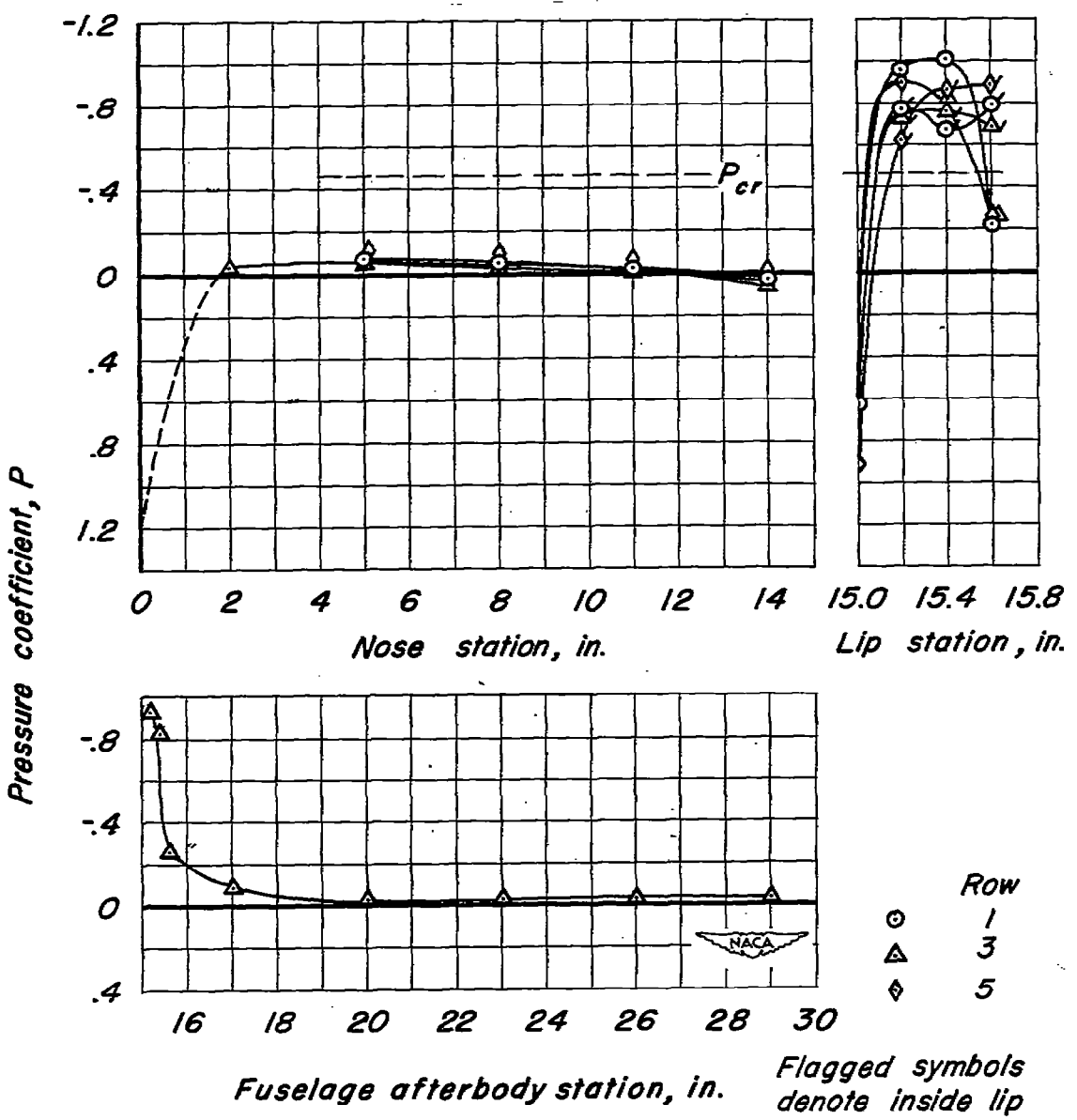

(a) M_o, 0.79; $\frac{m_1}{m_o}$, 0.93

Figure 21.—Pressure distribution along the body with scoop inlet; α, 0°.

[redacted]

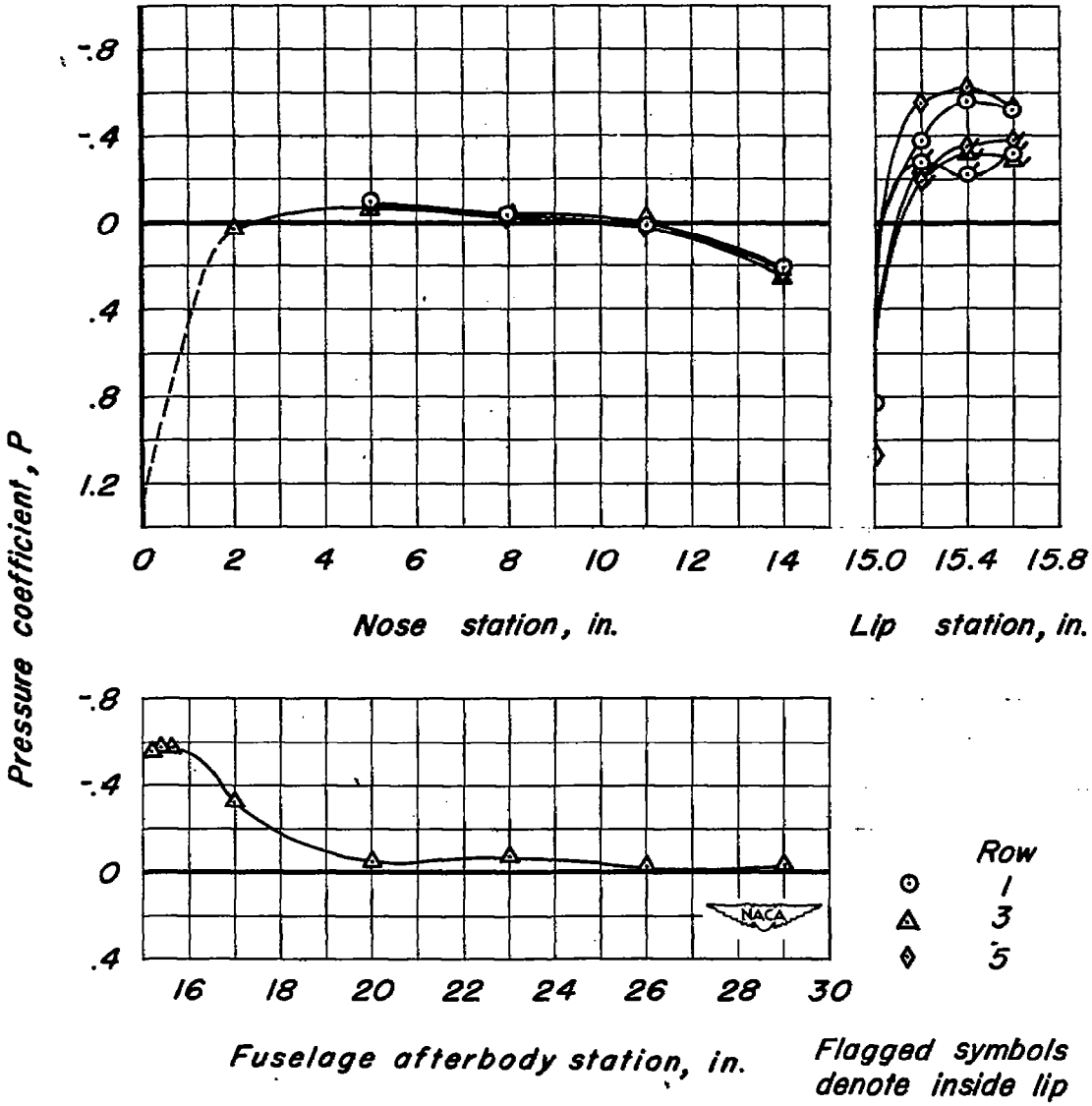

(b) M_o, 1.00; $\frac{m_1}{m_o}$, 0.88

Figure 21.—Continued.

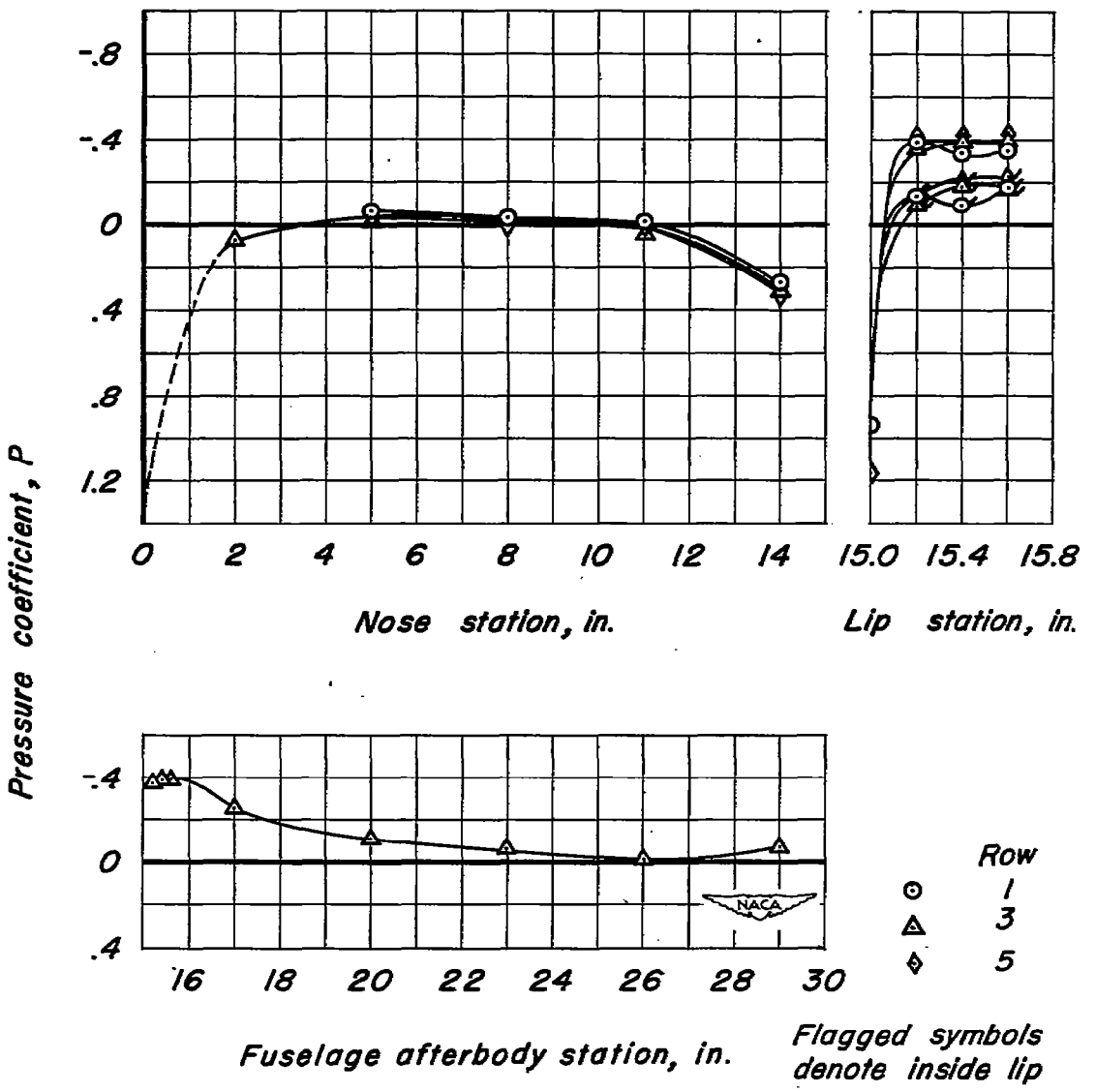

(c) M_o, 1.12; $\frac{m_1}{m_o}$, 0.88

Figure 21.—Concluded.

[redacted]

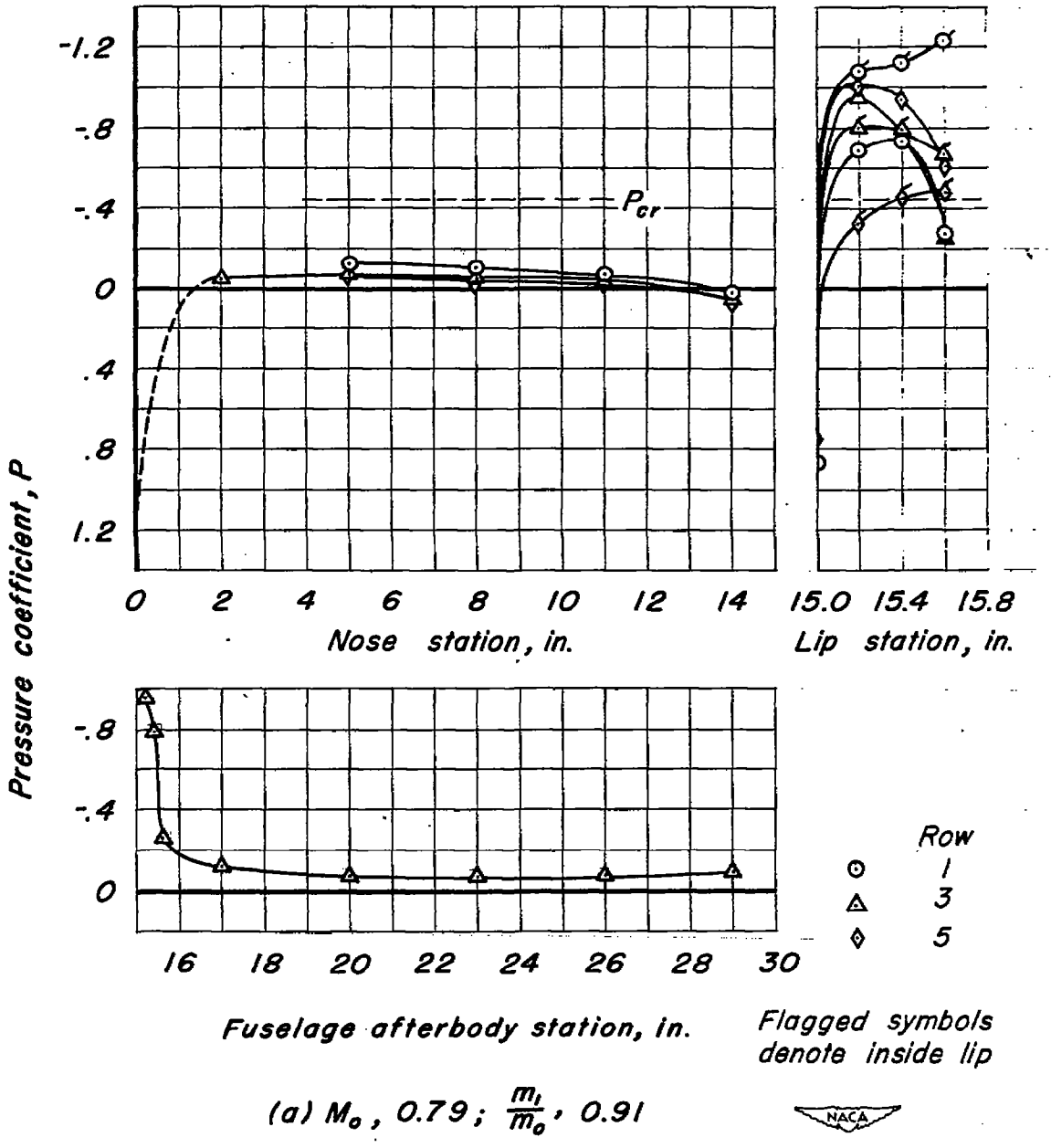

(a) M_o, 0.79; $\frac{m_1}{m_o}$, 0.91

Figure 22.—Pressure distribution along the body with scoop inlet; α, 6°.

[redacted]

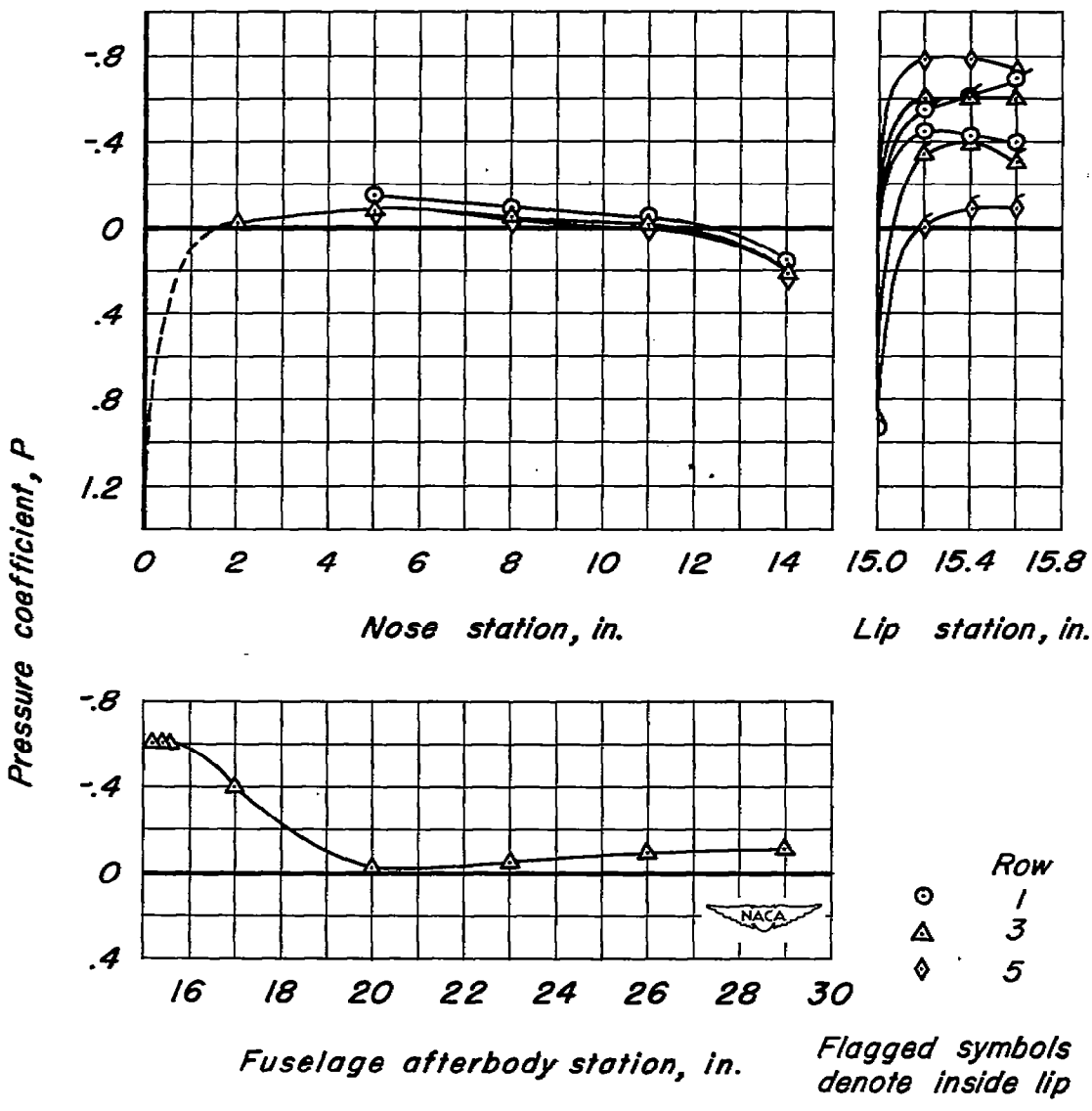

(b) M_o, 0.97; $\frac{m_1}{m_o}$, 0.87

Figure 22.—Continued.

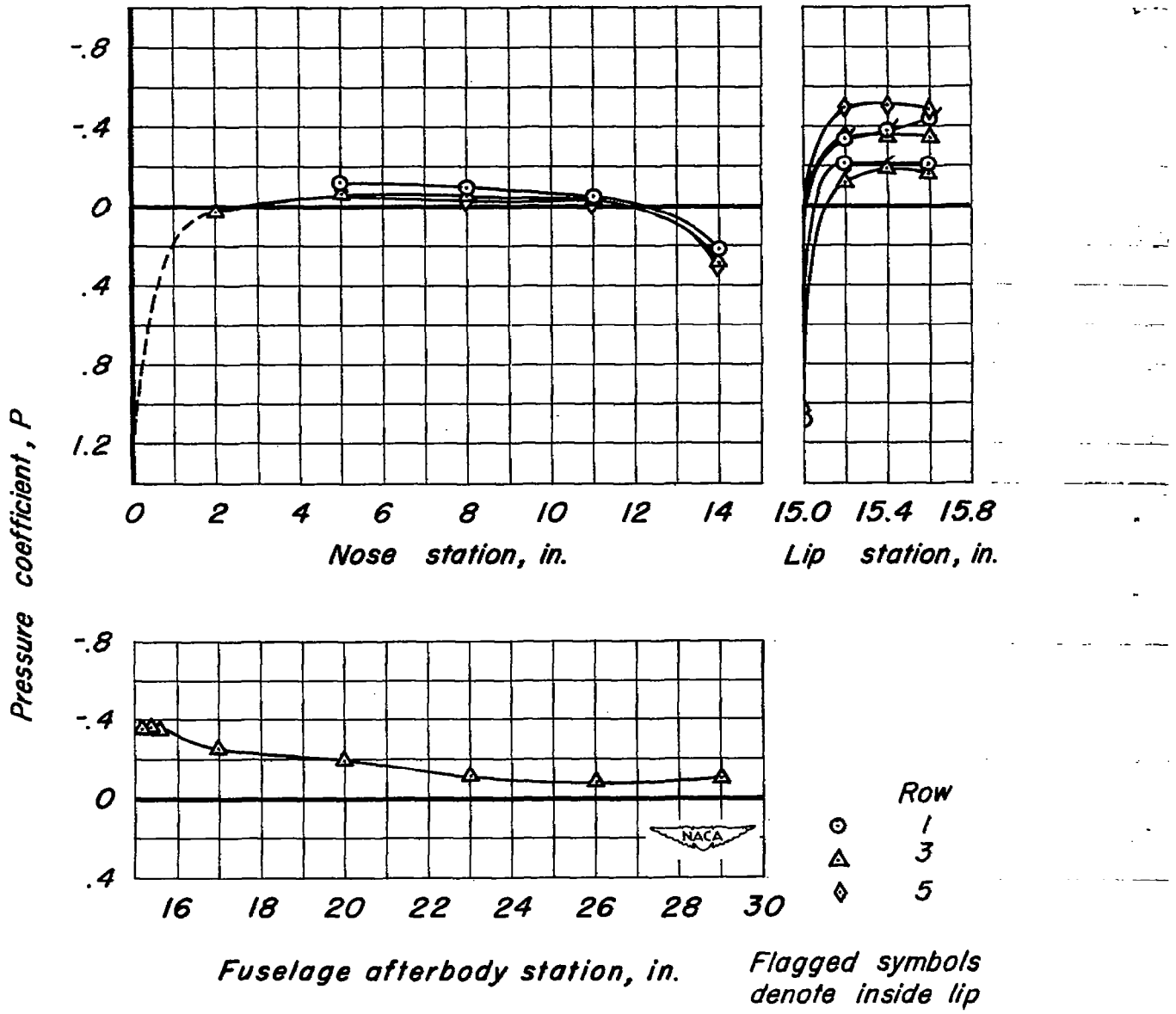

(c) M_o, 1.11; $\frac{m_1}{m_o}$, 0.87

Figure 22.–Concluded.

[redacted]

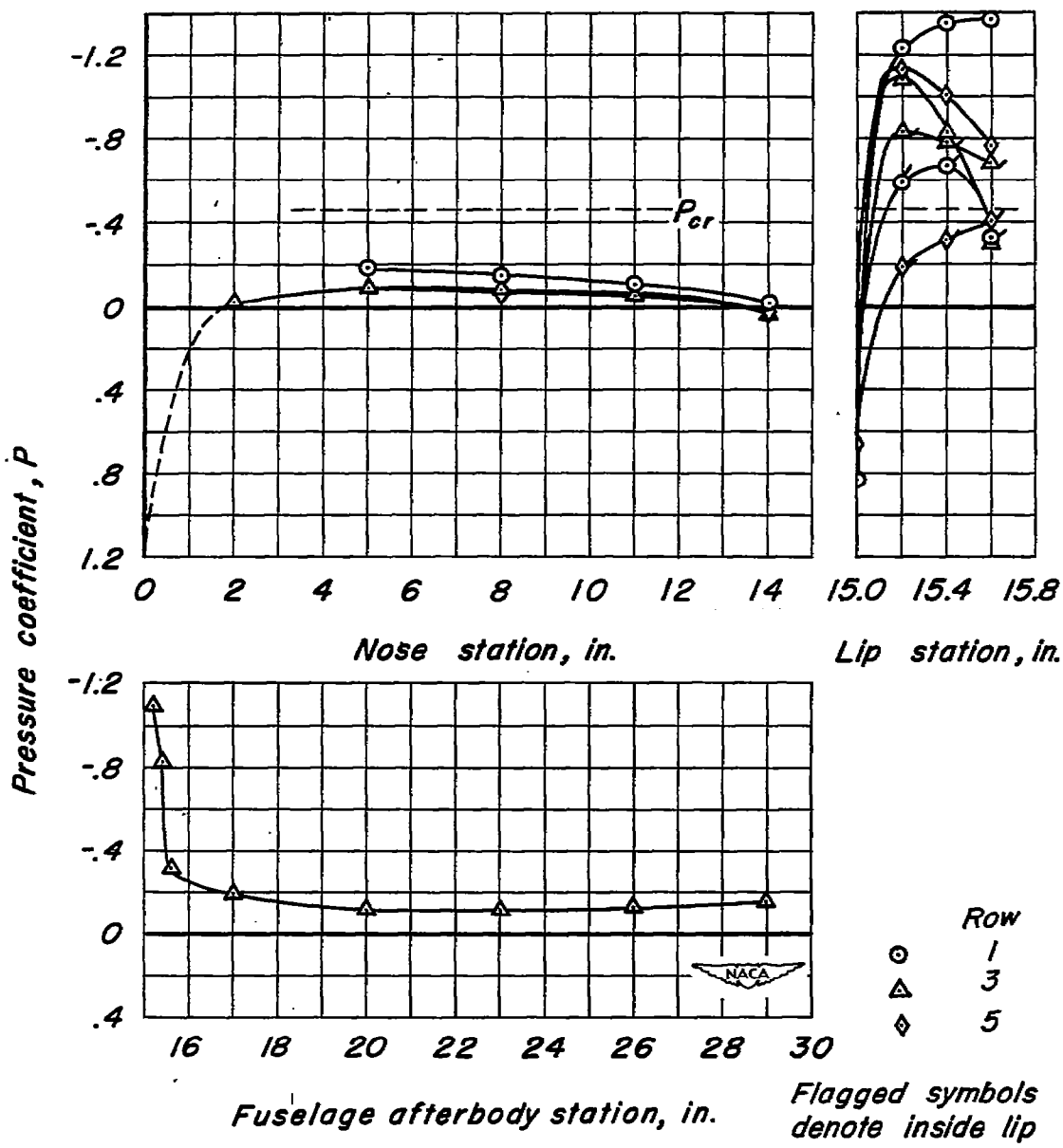

(a) M_o, 0.79; $\frac{m_1}{m_o}$, 0.91

Figure 23.–Pressure distribution along the body with scoop inlet; α, 9°.

[redacted]

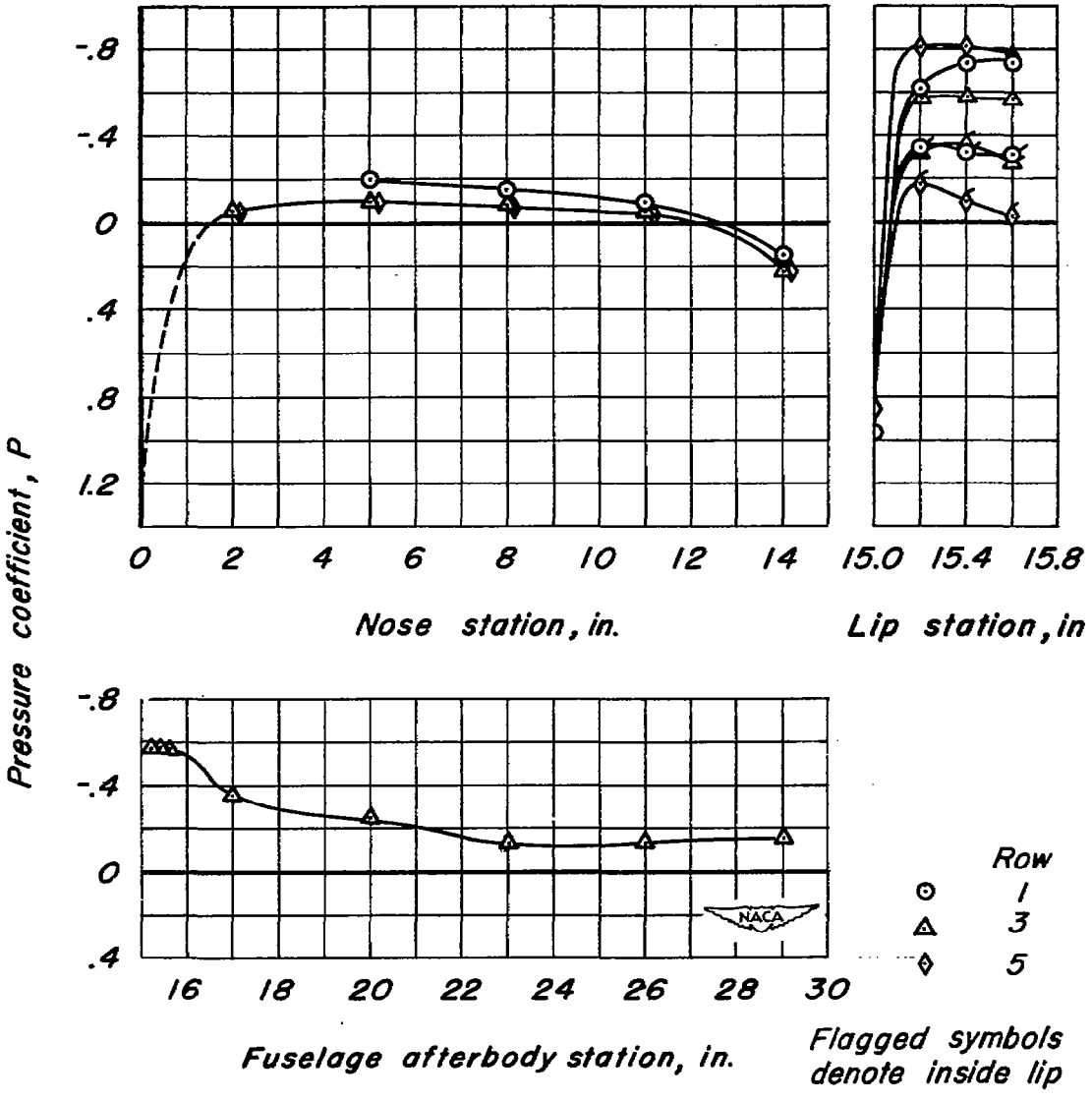

(b) M_o, 1.01; $\frac{m_1}{m_o}$, 0.85

Figure 23.—Continued.

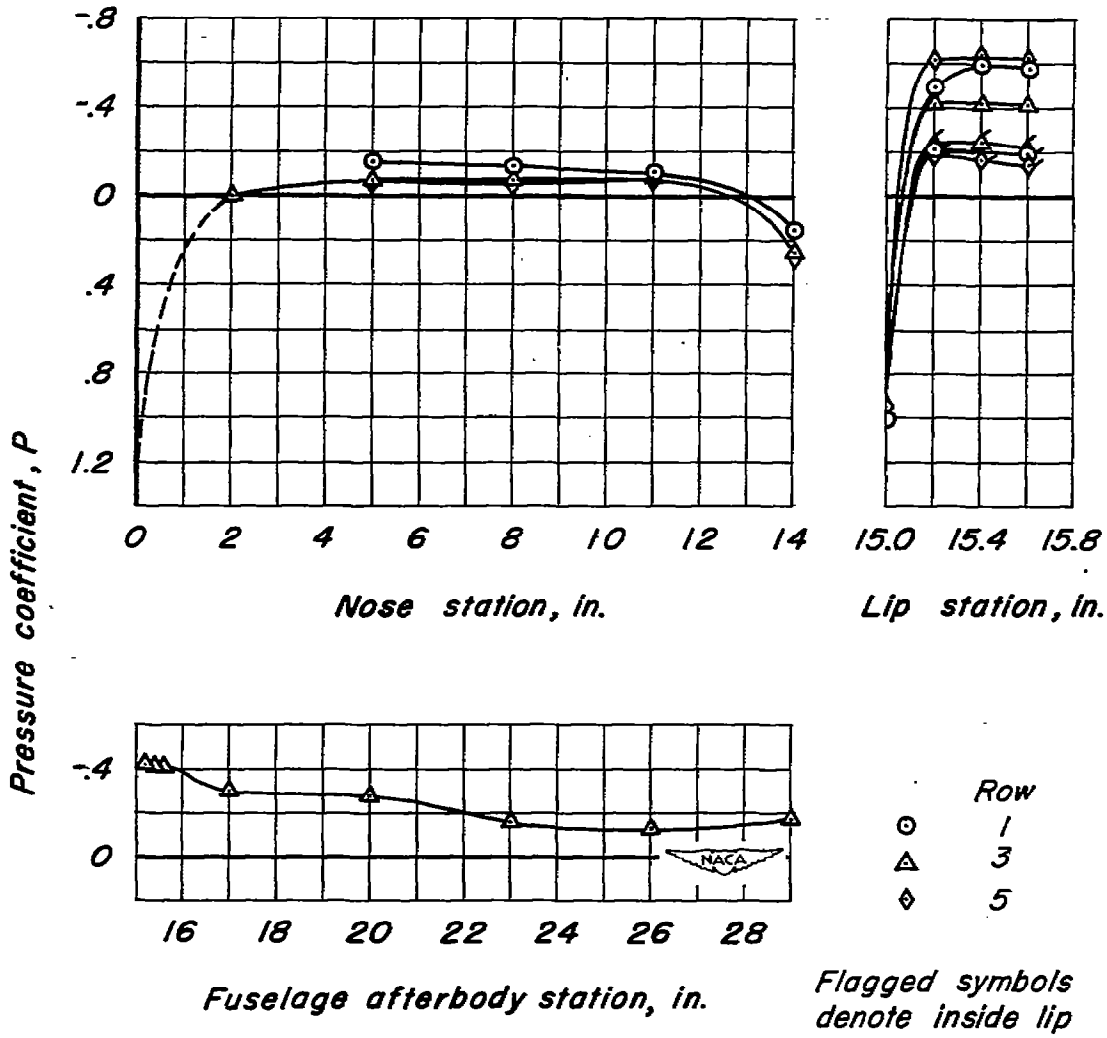

(c) M_o, 1.10; $\frac{m_1}{m_o}$, 0.85

Figure 23.—Concluded.

[redacted]

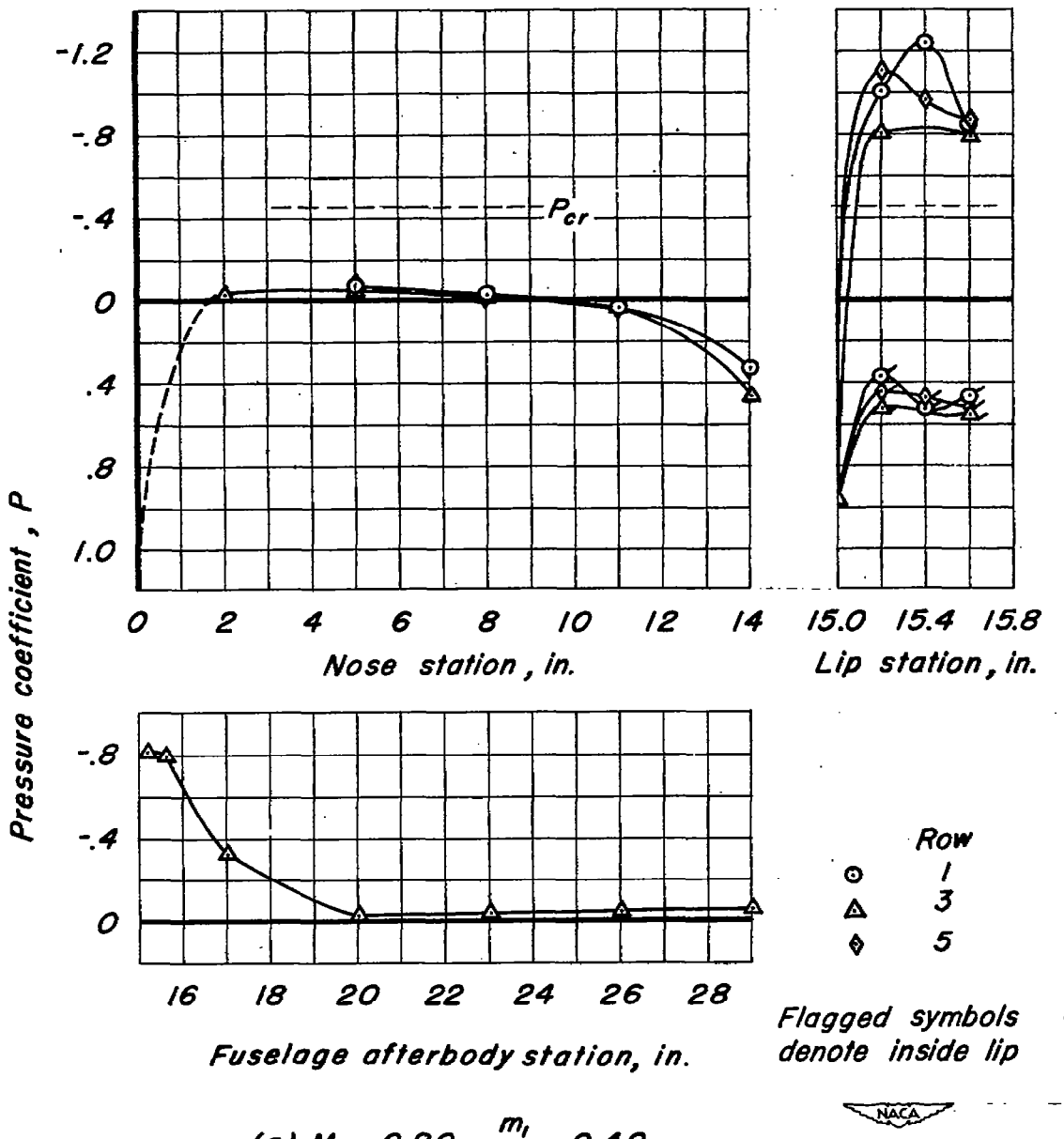

(a) M_o, 0.80; $\frac{m_1}{m_o}$, 0.40

Figure 24.— Pressure distribution along the body with scoop inlet; α, 0°

[redacted]

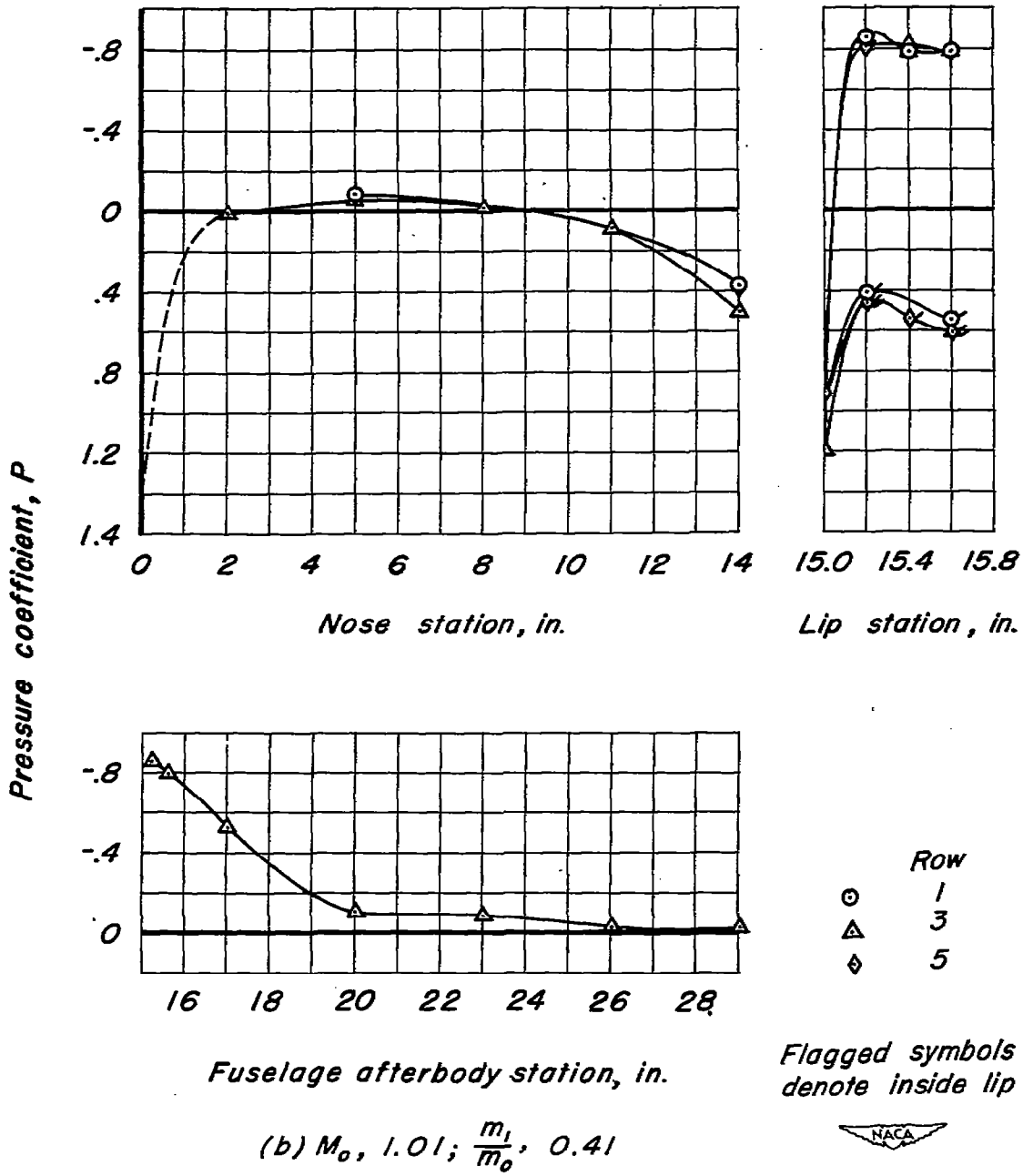

(b) M_o, 1.01; $\frac{m_1}{m_o}$, 0.41

Figure 24.– Continued.

[redacted]

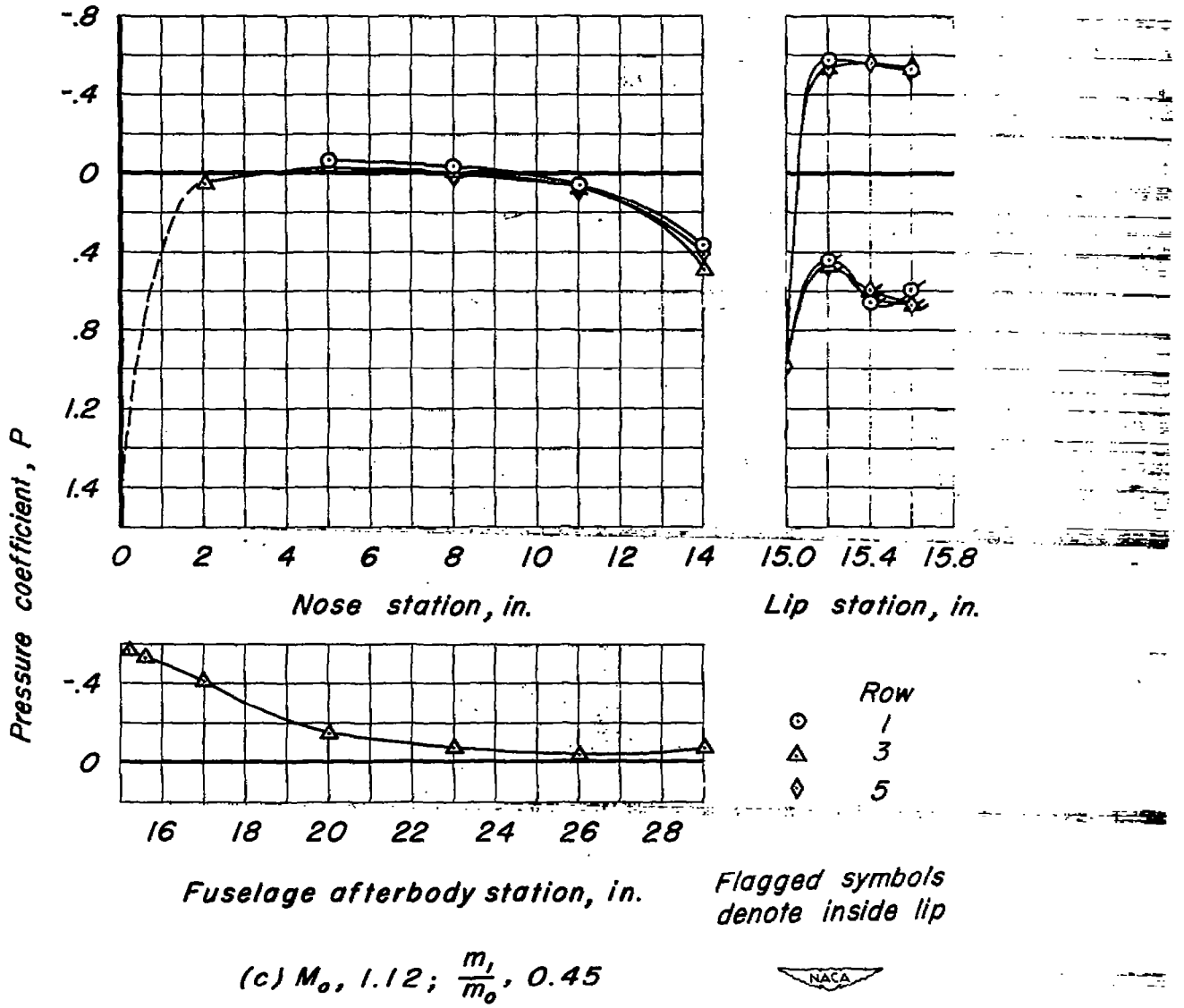

(c) M_o, 1.12; $\frac{m_1}{m_o}$, 0.45

Figure 24.—Concluded.

[redacted]

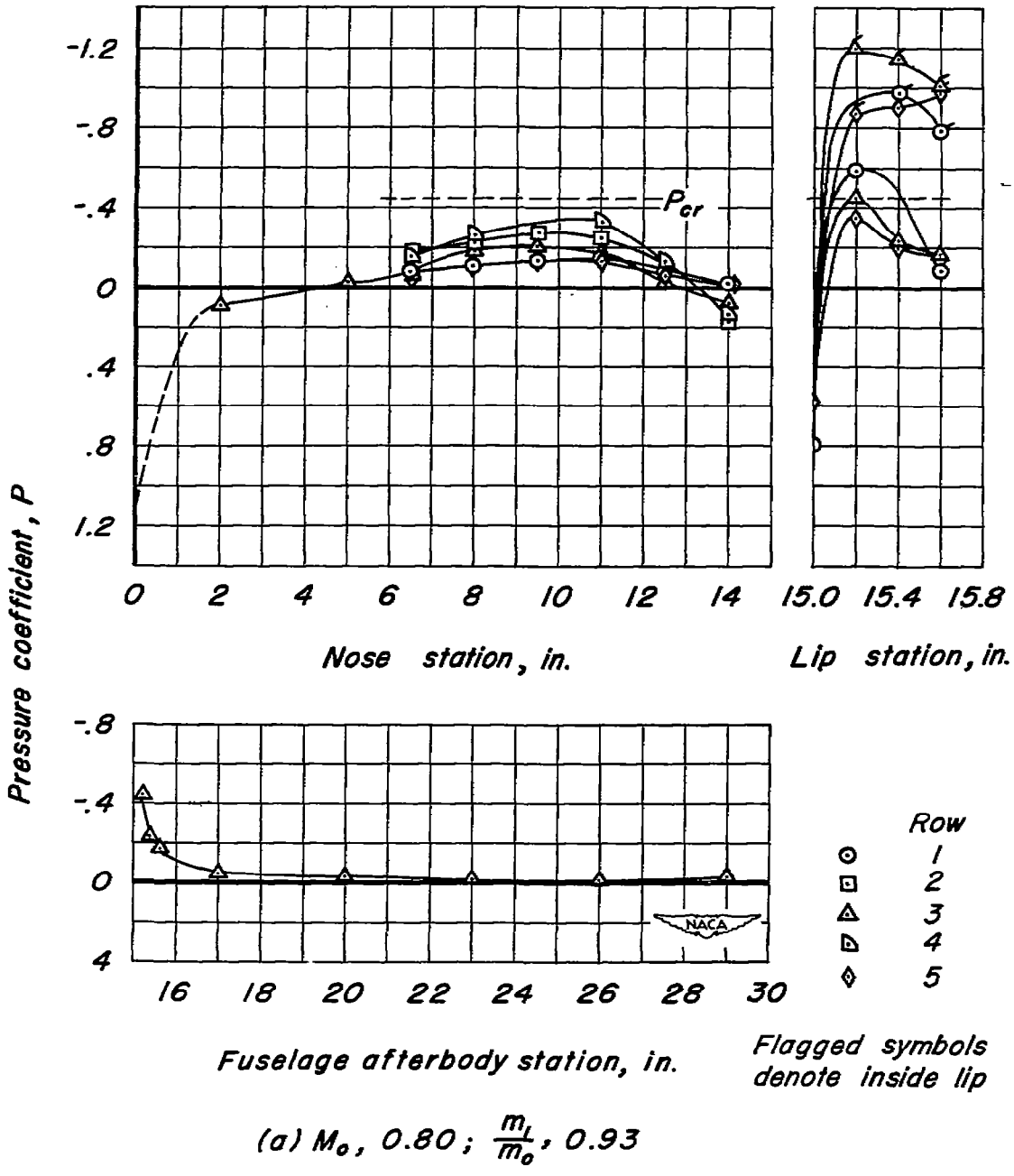

(a) M_o, 0.80; $\frac{m_l}{m_o}$, 0.93

Figure 25.—Pressure distribution along the body with submerged inlet; α, 0°

[redacted]

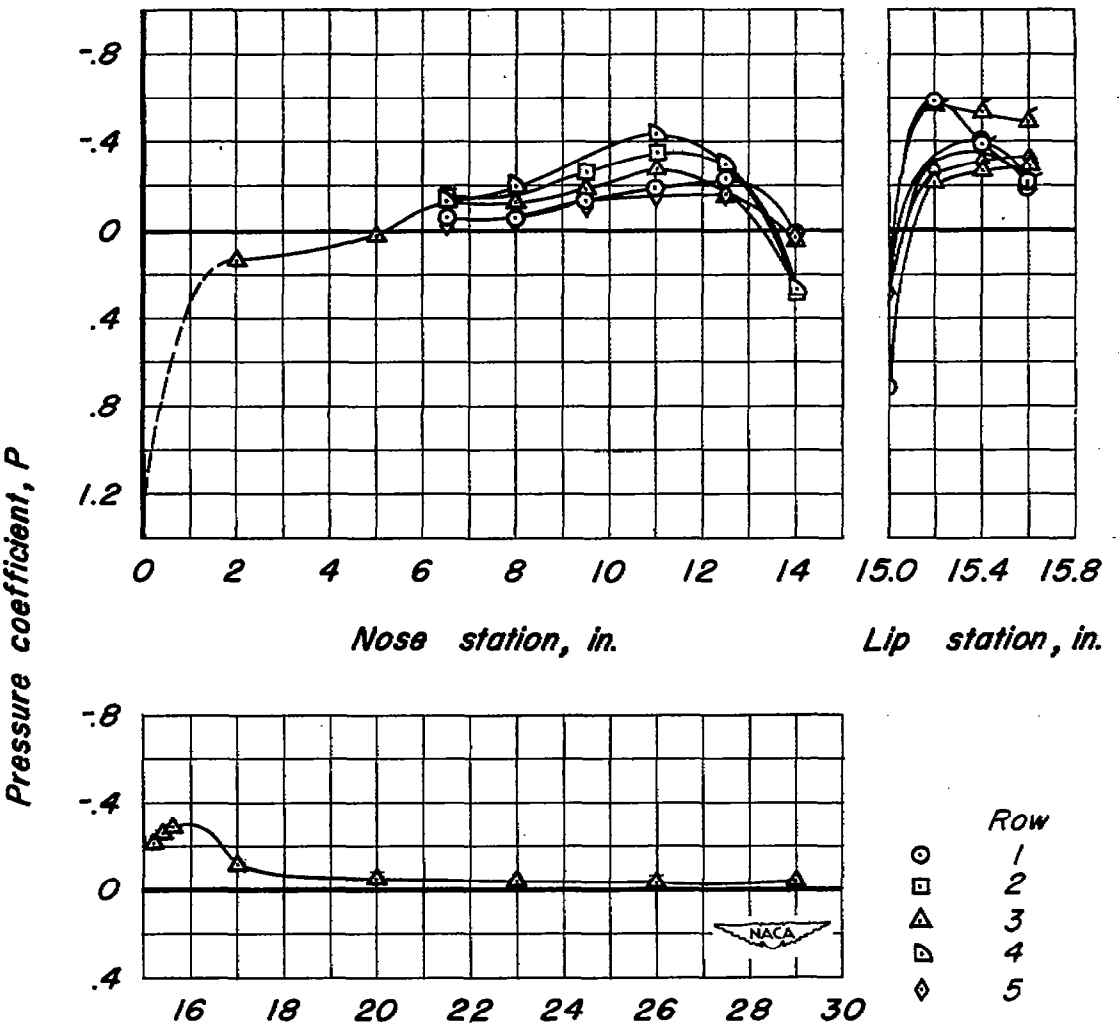

(b) M_o, 1.02; $\frac{m_1}{m_o}$, 0.88

Figure 25.-Continued.

[redacted]

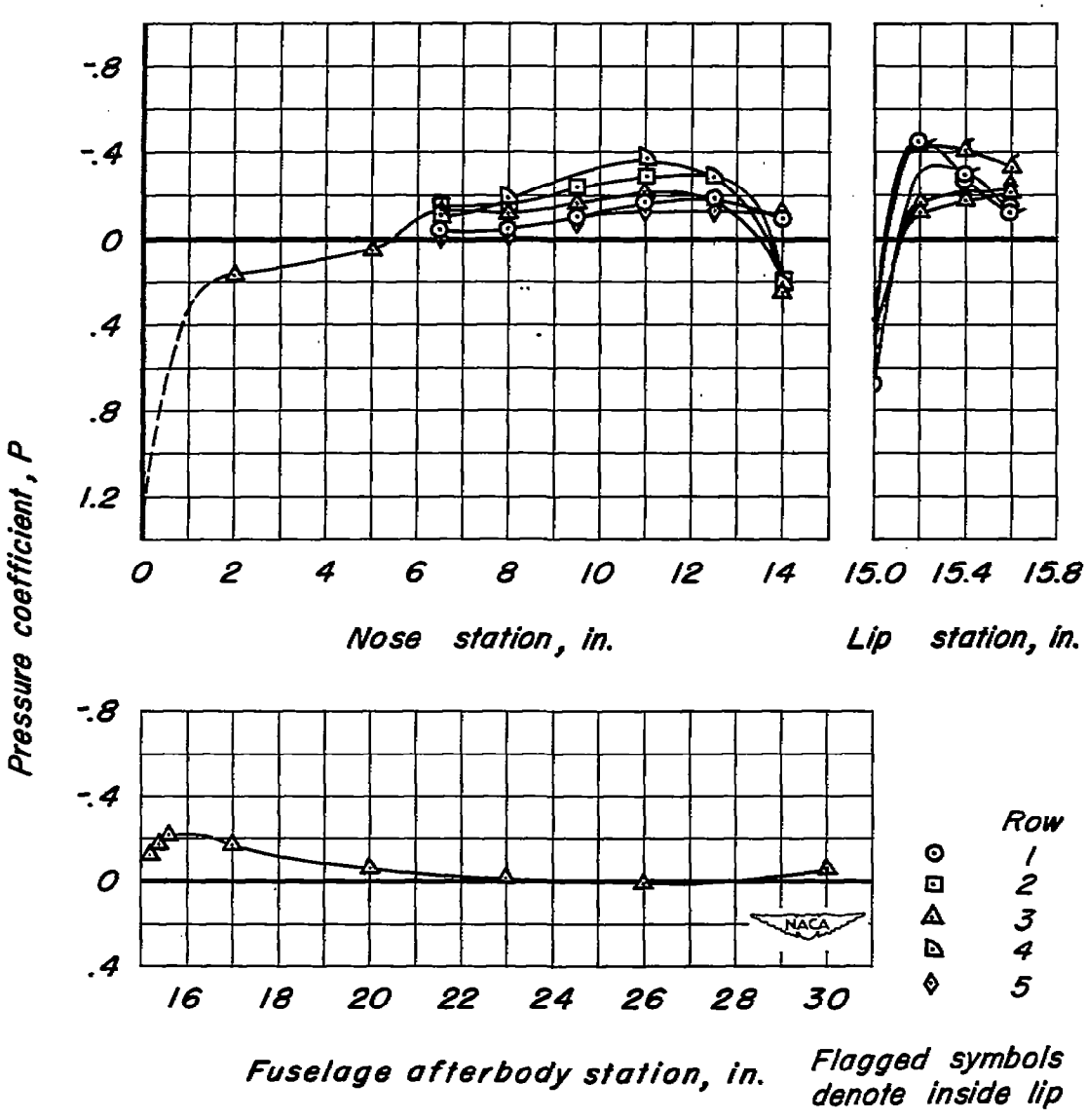

(c) M_o, 1.11; $\frac{m_1}{m_o}$, 0.88

Figure 25.—Concluded.

[redacted]

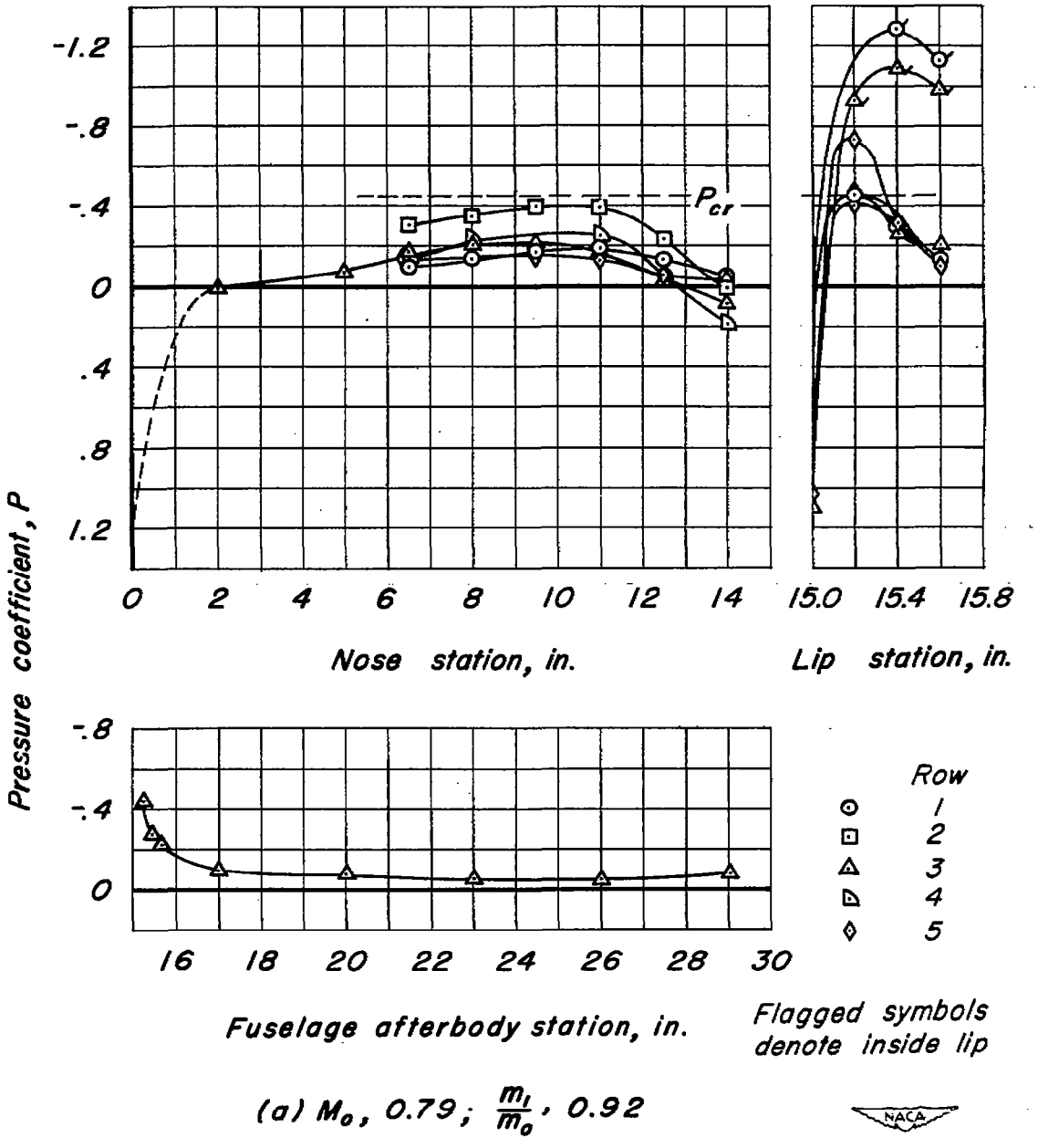

Figure 26.— Pressure distribution along the body with submerged inlet α, 6.°

[redacted]

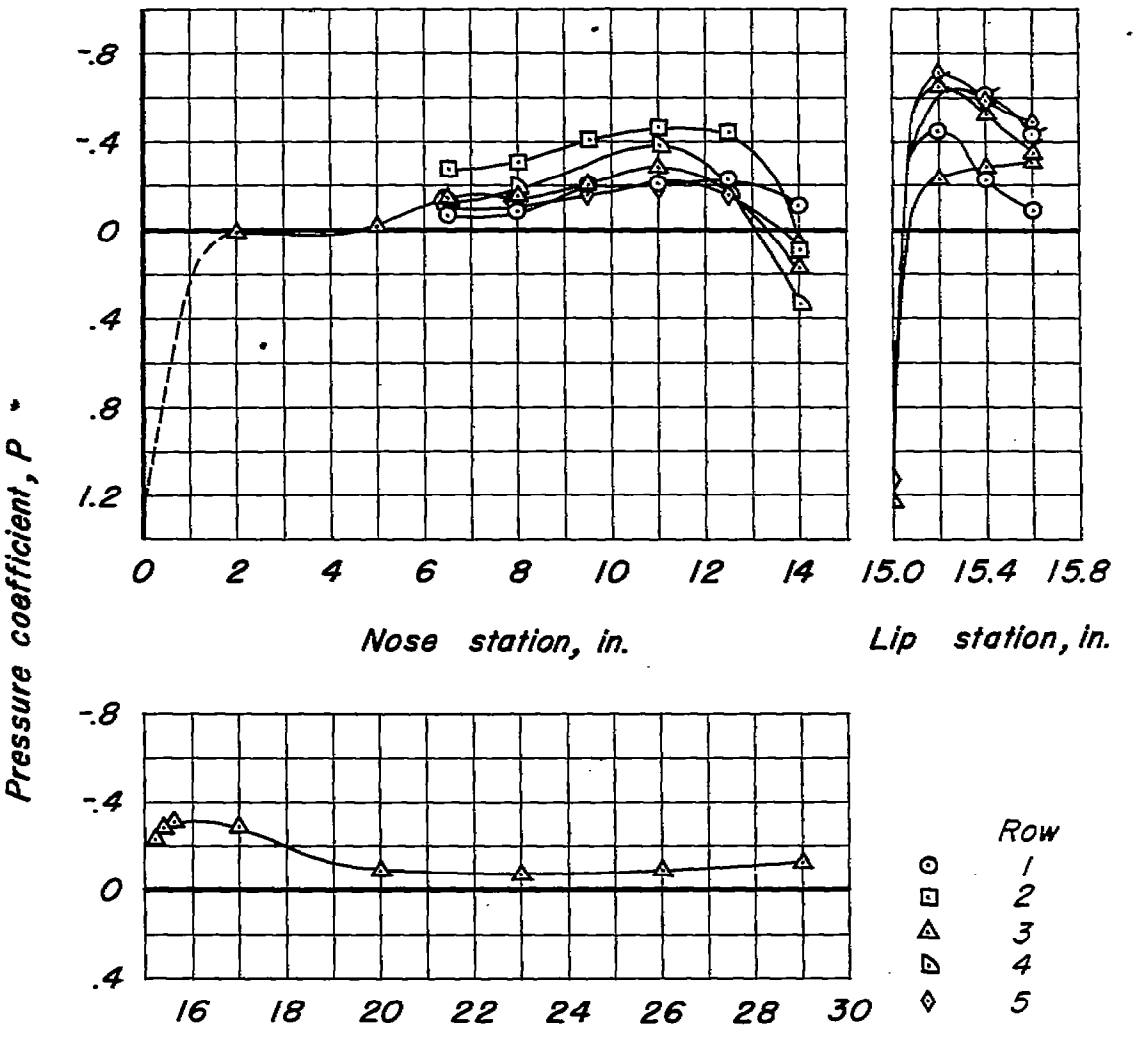

(b) M_o, 1.01, $\frac{m_1}{m_o}$, 0.87

Figure 26.–Continued.

[redacted]

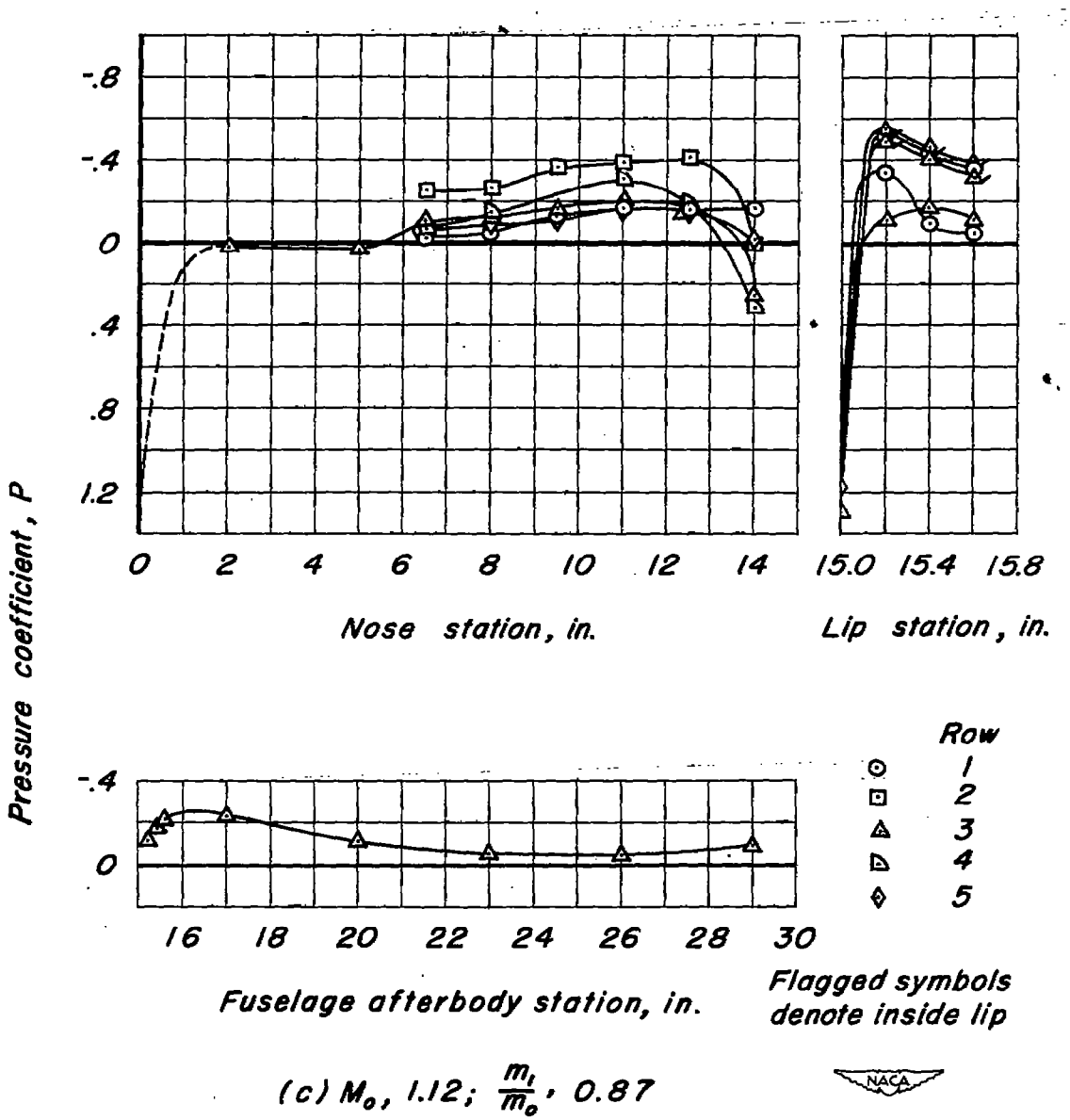

(c) M_o, 1.12; $\frac{m_1}{m_o}$, 0.87

Figure 26.—Concluded.

[redacted]

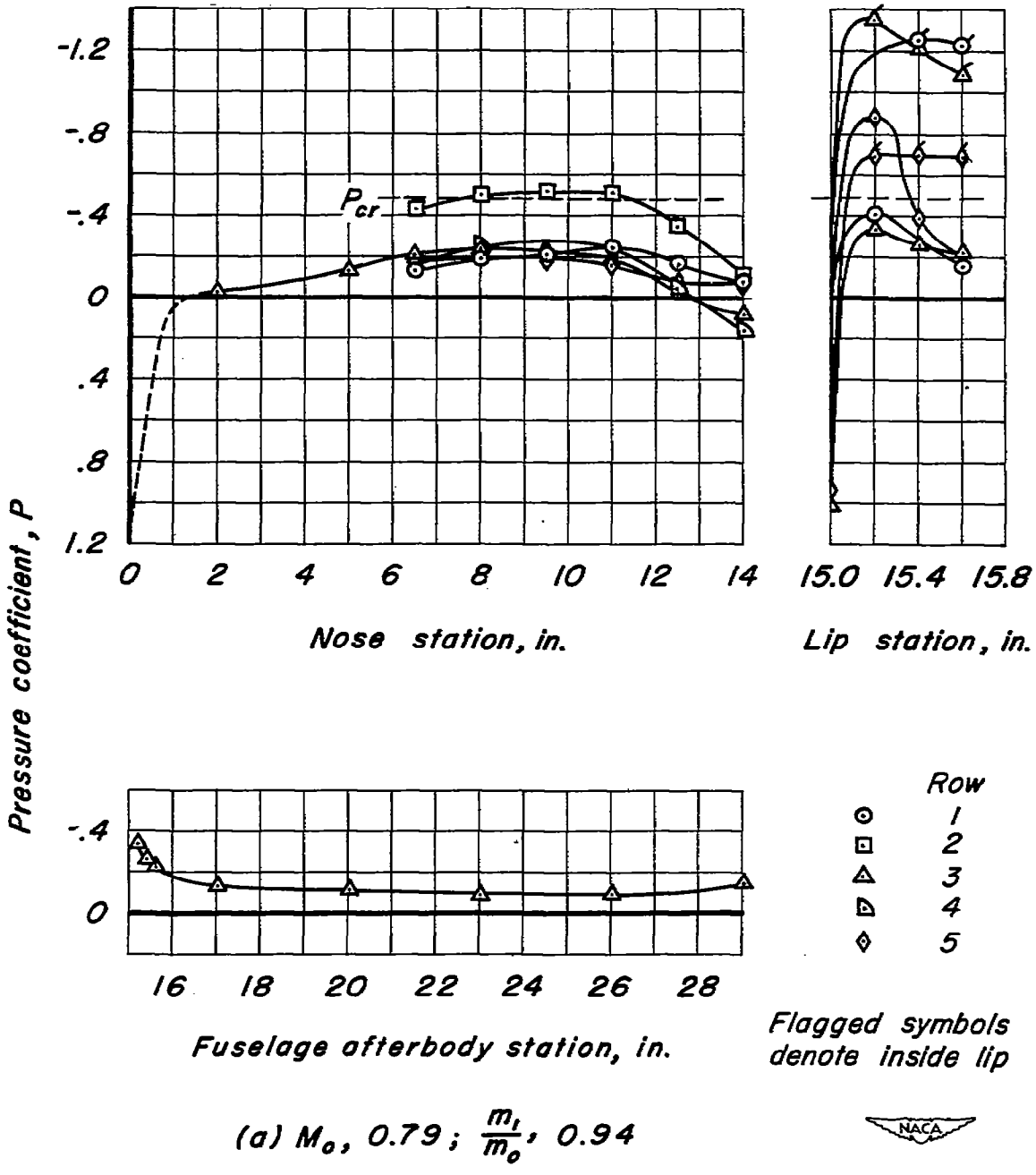

(a) M_o, 0.79; $\frac{m_1}{m_o}$, 0.94

Figure 27.— Pressure distribution along the body with submerged inlet; α, 9°

[redacted]

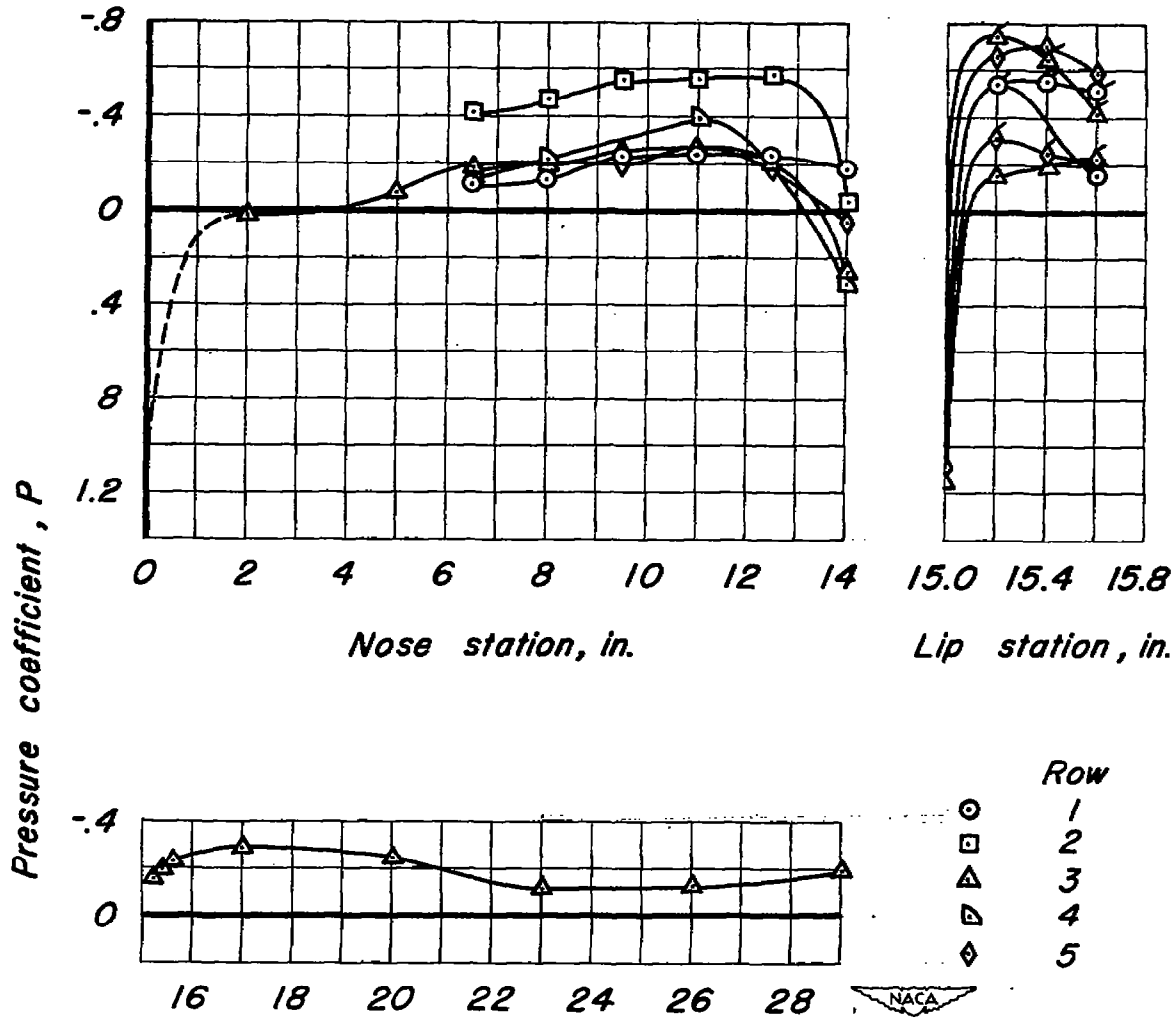

(b) M_o, 1.01; $\frac{m_1}{m_o}$, 0.83

Figure 27.—Continued.

[redacted]

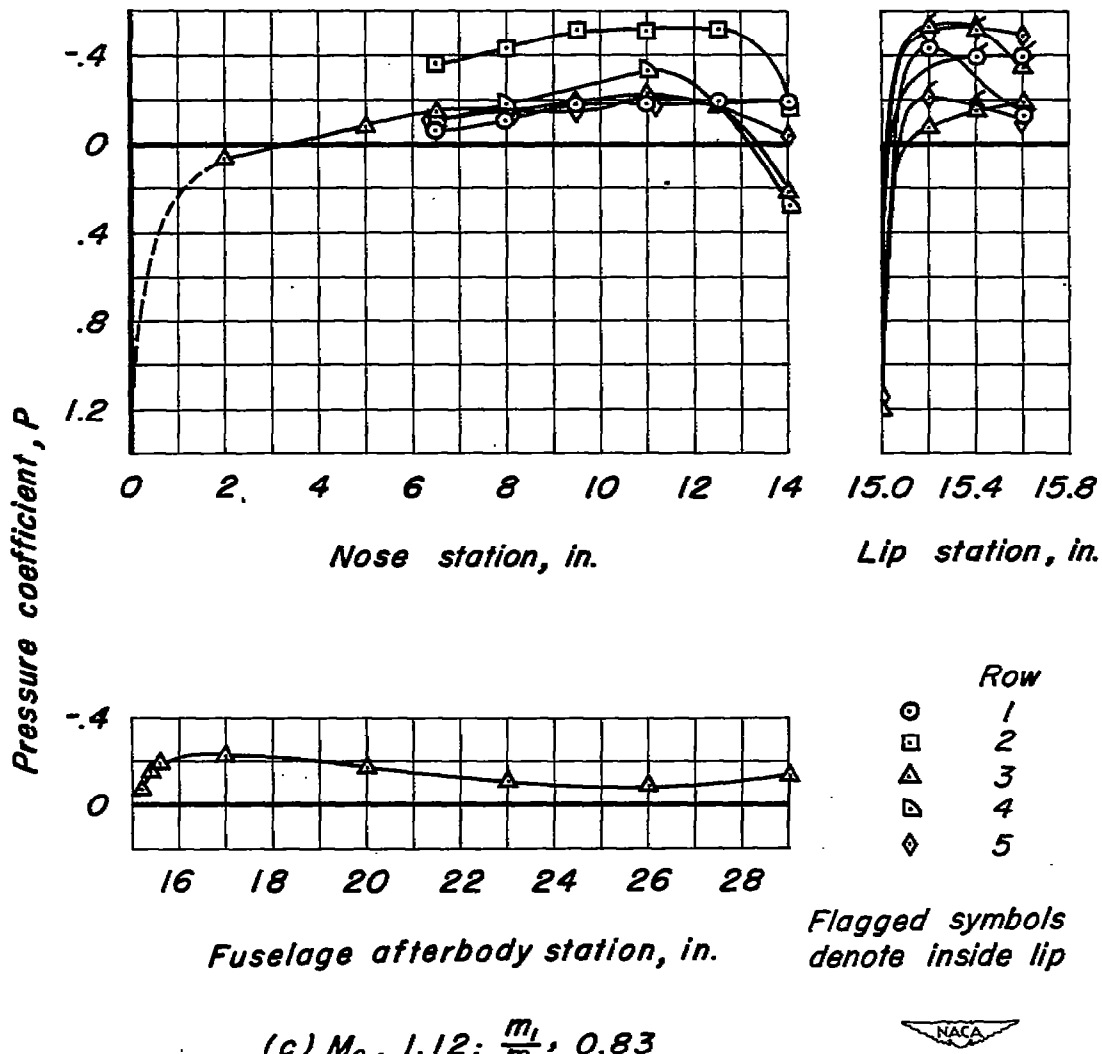

(c) M_o, 1.12; $\frac{m_1}{m_o}$, 0.83

Figure 27.—Concluded.

[redacted]

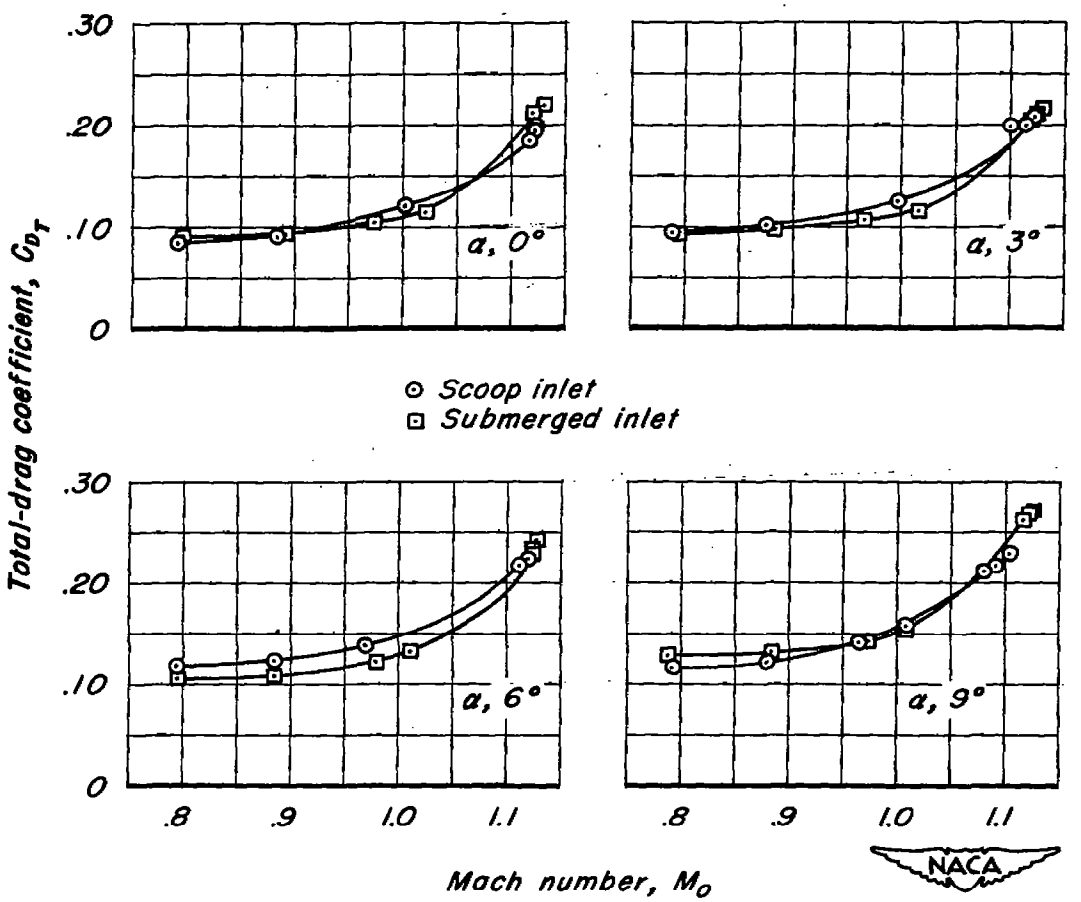

Figure 28.—Variation of total-drag coefficient with Mach number for the body at four angles of attack. Body with scoop inlet and with submerged inlet. $\frac{m_i}{m_o} \approx 0.88$.

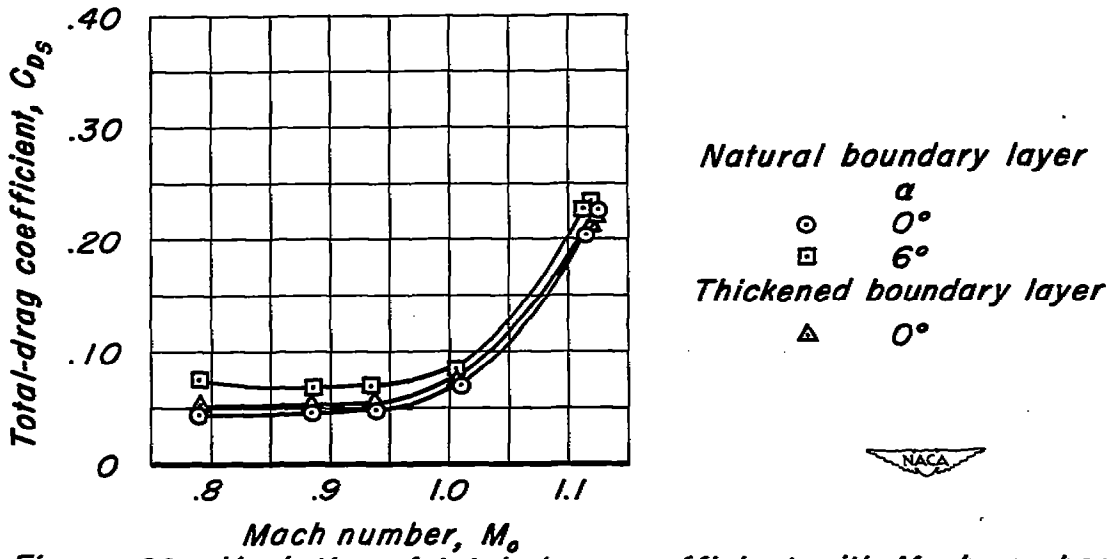

Figure 29.—Variation of total-drag coefficient with Mach number for the solid body with a normal and a thickened boundary layer; α, 0° and 6°.

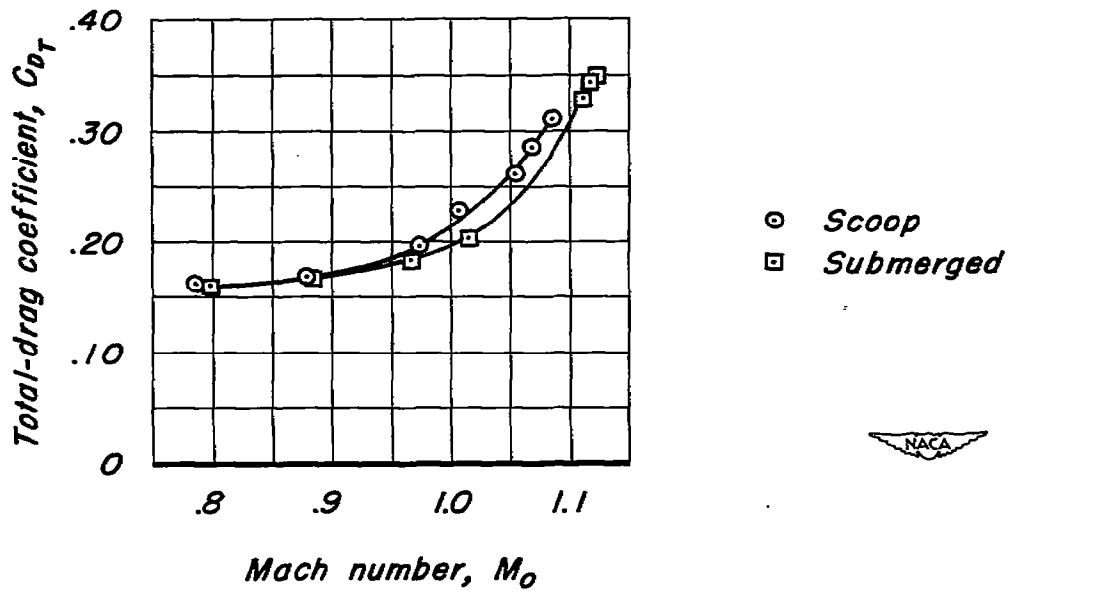

Figure 30.-Variation of total-drag coefficient with Mach number for the model with scoop inlet and with submerged inlet; $\frac{m_i}{m_o}$, 0; α, 0°.

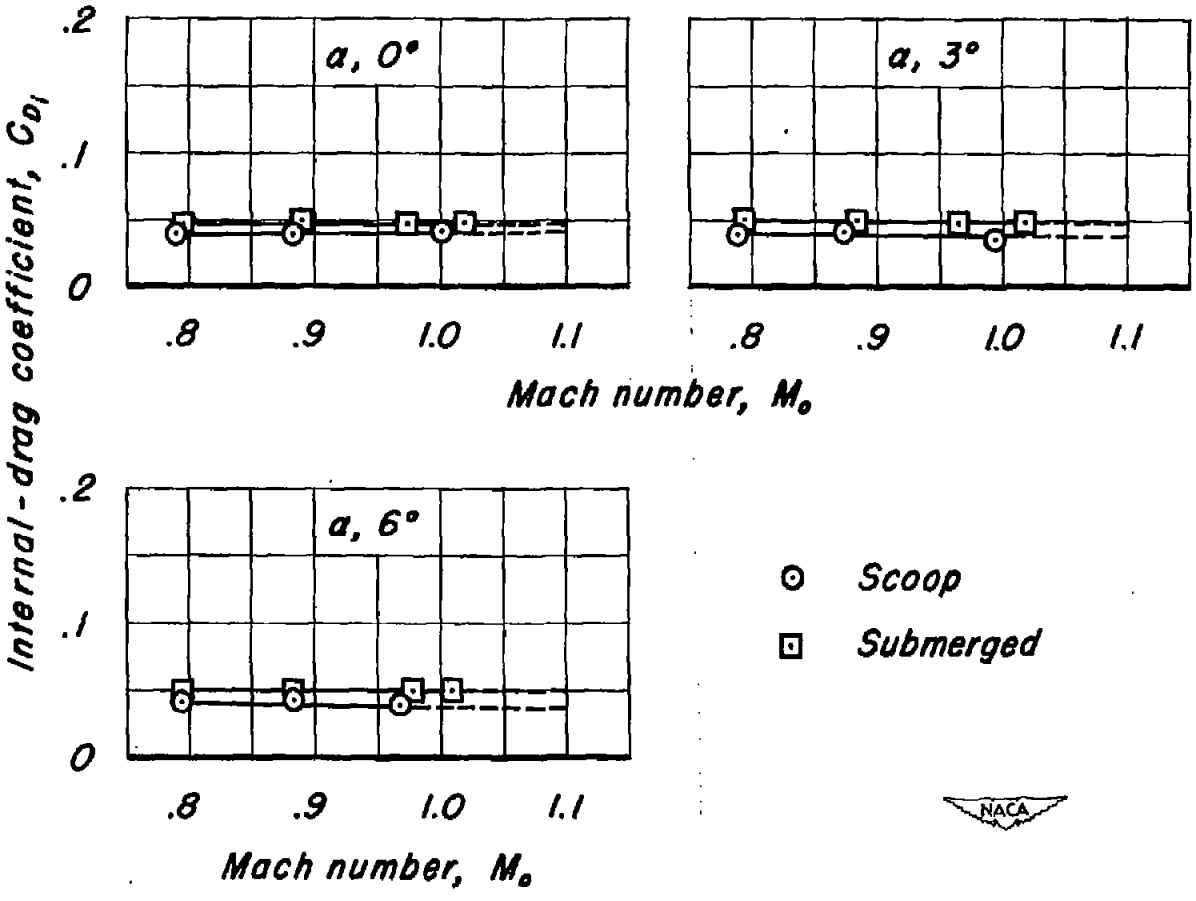

Figure 31.—Variation of internal-drag coefficient with Mach number at the exit of the scoop inlet and the submerged inlet at three angles of attack; $\frac{m_i}{m_o}=0.88$.

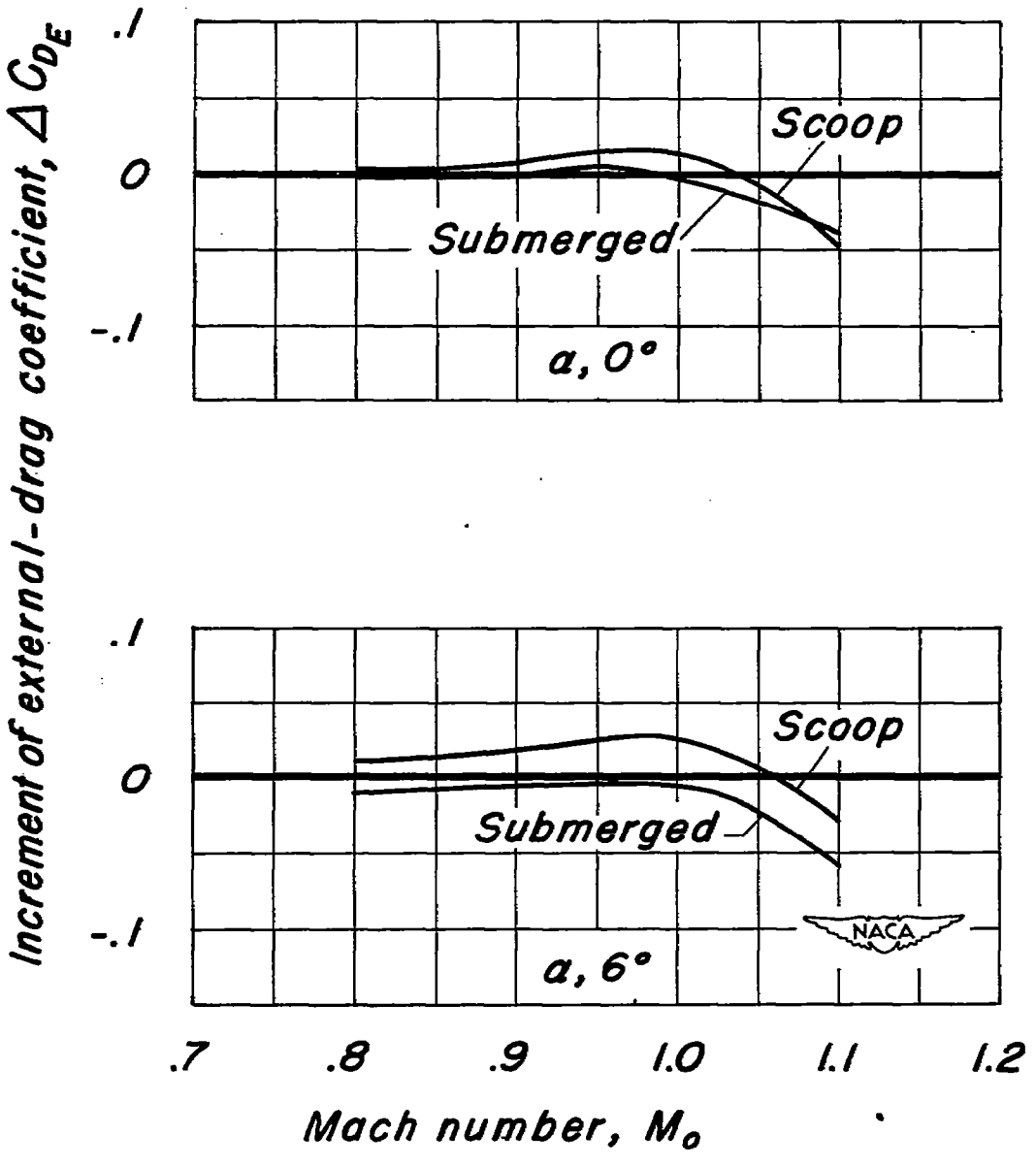

Figure 32.–Variation of increment of external-drag coefficient with Mach number for the scoop inlet and the submerged inlet at two angles of attack; $\frac{m_1}{m_o}=0.88$.

[redacted]